



HAL
open science

Ninety degrees pitch angle enhancements of suprathermal electrons associated with interplanetary shocks

P. Kajdič, B. Lavraud, A. Zaslavsky, X. Blanco-Cano, J.-A. Sauvaud, A.
Opitz, L. Jian, M. Maksimovic, J. Luhmann

► **To cite this version:**

P. Kajdič, B. Lavraud, A. Zaslavsky, X. Blanco-Cano, J.-A. Sauvaud, et al.. Ninety degrees pitch angle enhancements of suprathermal electrons associated with interplanetary shocks. *Journal of Geophysical Research Space Physics*, 2014, 119 (9), pp.7038-7060. 10.1002/2014JA020213 . hal-02544445

HAL Id: hal-02544445

<https://hal.science/hal-02544445>

Submitted on 25 Nov 2021

HAL is a multi-disciplinary open access archive for the deposit and dissemination of scientific research documents, whether they are published or not. The documents may come from teaching and research institutions in France or abroad, or from public or private research centers.

L'archive ouverte pluridisciplinaire **HAL**, est destinée au dépôt et à la diffusion de documents scientifiques de niveau recherche, publiés ou non, émanant des établissements d'enseignement et de recherche français ou étrangers, des laboratoires publics ou privés.

Copyright

RESEARCH ARTICLE

10.1002/2014JA020213

Ninety degrees pitch angle enhancements of suprathermal electrons associated with interplanetary shocks

Key Points:

- New type of suprathermal electron distributions at IP shocks is analyzed
- IP shock properties do not correlate with the presence of these distributions
- Correlation exists between the distributions and the wave activity at IP shocks

Correspondence to:

P. Kajdič,
kajdic@gmail.com

Citation:

Kajdič, P., B. Lavraud, A. Zaslavsky, X. Blanco-Cano, J.-A. Sauvaud, A. Opitz, L. K. Jian, M. Maksimovic, and J. G. Luhmann (2014), Ninety degrees pitch angle enhancements of suprathermal electrons associated with interplanetary shocks, *J. Geophys. Res. Space Physics*, 119, 7038–7060, doi:10.1002/2014JA020213.

Received 28 MAY 2014

Accepted 13 AUG 2014

Accepted article online 15 AUG 2014

Published online 2 SEP 2014

P. Kajdič^{1,2,3}, B. Lavraud^{1,2}, A. Zaslavsky⁴, X. Blanco-Cano⁵, J.-A. Sauvaud^{1,2}, A. Opitz³, L. K. Jian^{6,7}, M. Maksimovic⁴, and J. G. Luhmann⁸

¹Université de Toulouse, UPS-OMP, IRAP, Toulouse, France, ²CNRS, IRAP, Toulouse, France, ³European Space Research and Technology Centre, European Space Agency, Noordwijk, Netherlands, ⁴LESIA, Observatoire de Paris-CNRS-Université Pierre et Marie Curie-Université Denis Diderot, Paris, France, ⁵Instituto de Geofísica, Ciencias Espaciales, Universidad Nacional Autónoma de México, Mexico City, Mexico, ⁶Department of Astronomy, University of Maryland, College Park, Maryland, USA, ⁷NASA Goddard Space Flight Center, Greenbelt, Maryland, USA, ⁸Space Sciences Laboratory, University of California, Berkeley, California, USA

Abstract We report the results of the first systematic analysis of 90° pitch angle (PA) enhancements or the ring distributions of suprathermal ($E \sim 70$ eV–2 keV) electrons at interplanetary (IP) shocks. We analyze 2 h time intervals around 232 IP shocks observed by the two STEREO spacecraft between 2007 and 2011. The ring distributions were detected downstream of 114 events (49%). In 52 (22.4%) cases they were detected at the shock ramp. We also found 90° enhancements upstream of 11 (4.7%) events. Statistical analysis of basic shock properties did not reveal substantial differences between the shocks that are associated with the enhancements and those that are not. The data from the STEREO/WAVES instruments revealed that the 90° PA enhancements tend to be associated with magnetic and electric field fluctuations. Although at this point we do not have a satisfactory explanation for the mechanism that produces these distributions, our findings suggest that wave-particle interactions play a role, while pure focusing and mirroring effects due to adiabatic motion of electrons across the shock fronts cannot fully account for the observations.

1. Introduction

The electron distribution function in the regular solar wind (SW) is composed of three main components: a core, a halo, and a strahl [e.g., *Montgomery et al.*, 1968; *Feldman et al.*, 1975, 1978; *Rosenbauer et al.*, 1976; *Maksimovic et al.*, 2005]. The core electrons account for $\sim 95\%$ of all the electrons in the SW. They represent the coolest ($T_c \sim 10$ eV) component and are marginally collisional at 1 AU [*Phillips and Gosling*, 1990]. The electrons with energies above ~ 70 eV are called suprathermal electrons. Below 2 keV they compose an isotropic halo and a narrow and intense antisunward directed beam known as the strahl. Suprathermal electrons are collisionless [e.g., *Scudder and Olbert*, 1979a, 1979b; *Fairfield and Scudder*, 1985; *Ogilvie et al.*, 2000]. In addition to the three main components, *Lin* [1998] reported the existence of a very tenuous population, called the “superhalo,” which is composed of electrons with energies $\gtrsim 2$ keV and appears to be isotropic.

The origin of suprathermal populations has been discussed a lot in the literature. It has been proposed that a portion of electrons may be energized in the corona through resonant interaction with whistler waves [e.g., *Vocks and Mann*, 2003]. Farther out in interplanetary (IP) space the diverging and decreasing interplanetary magnetic field (IMF) tends to focus these electrons into a narrow strahl [e.g., *Rosenbauer et al.*, 1976]. However, in situ observations show strahl widths that are larger than those expected from pure adiabatic focusing effects [e.g., *Anderson et al.*, 2012]. This means that some kind of strahl-scattering mechanism must exist in the IP space. Binary collisions of suprathermal electrons either with core electrons or with ions are practically negligible and hence cannot be responsible for the observed strahl widths [*Lemons and Feldman*, 1983; *Maksimovic et al.*, 2005; *Štverák et al.*, 2009].

Resonant interactions of the strahl electrons with whistler waves in IP space have been proposed as one of the main candidates for pitch angle (PA) diffusion of the strahl electrons and the formation of the halo population. It is thought that electron core temperature anisotropy may give rise to the whistler anisotropy instability, which can then scatter the relatively low-energy strahl electrons through cyclotron resonance [*Saito and Gary*, 2007a]. On the other hand, sunward propagating whistler fluctuations with a broadband

power spectrum can scatter strahl electrons in a much wider energy range [Vocks *et al.*, 2005; Saito and Gary, 2007a, 2007b; Pagel *et al.*, 2007].

Other types of suprathermal electron populations were also observed in the past in association with different phenomena in the solar wind. We briefly describe them in the following sections.

1.1. Other Suprathermal Electron Populations on Open IMF Lines

Apart from the above electron populations, Gosling *et al.* [2001a] observed strong depletions in SW electron halo distributions on open IMF lines. These were centered at and approximately symmetric about 90° PA. Gosling *et al.* [2001a] found these distributions to occur in their data sets ~10% of the time. The latter value was found to depend upon the exact threshold used for identification of depletions [e.g., Lavraud *et al.*, 2010]. The depletions were often accompanied by enhanced sunward flows of suprathermal electrons centered at some acute PAs (between 0° and 90°), called the conics, and antisunward propagating populations at PAs complementary to those of the conics, called the shoulders. All three types of populations of suprathermal electrons were attributed to first heating and scattering of a part of the strahl population at *B* field enhancements or at IP shocks at larger heliospheric distances beyond that of the spacecraft, and then to the focusing and mirroring effects during the propagation of sunward scattered electrons along the *B* field lines.

1.2. Populations Associated With Different Structures in the SW

Electron distributions within large-scale structures in the SW, such as interplanetary coronal mass ejections (ICMEs) and stream interaction regions (SIRs), including corotating interaction regions (CIRs) and IP shocks, deviate strongly from distributions in the quiet SW. This is also the case for those regions that are magnetically connected to either IP or planetary shocks, such as the foreshocks and the downstream sheath regions.

Velocity distribution functions (VDFs) of electrons upstream from, at, and downstream of the Earth's bow shock have been studied by several authors [e.g., Feldman *et al.*, 1982a, 1982b, 1983a]. Upstream of the bow shock, these authors observed backstreaming, sunward propagating electron populations which were either field aligned (PA ~0°) or exhibited twin peaks (at some acute PA) centered on the *B* field direction. In the shock transition, the electrons are accelerated downstream, parallel to the *B* field by the cross-shock potential, while at the same time the adiabatic effects tend to conserve their transverse linear momentum by diminishing their parallel velocity components and increasing their velocities perpendicular to the *B* field. The distributions commonly show peaks that are offset from the bulk speed toward the downstream region, and they gradually develop flattops. Downstream of the bow shock, the electron distributions usually exhibit flattops up to some energy E_0 , which tends to be in the range 30 eV–150 eV. Often the electron VDFs are enhanced along the *B* direction for $E < E_0$ while their values are diminished along *B* for $E > E_0$.

Sunward streaming suprathermal electrons (aligned with the *B* field direction), conics (at acute PAs), and symmetric 90° PA depletions were observed in connection with SIRs including CIRs [Gosling *et al.*, 1993; Phillips *et al.*, 1996; Gosling *et al.*, 2001b; Steinberg *et al.*, 2005; Lavraud *et al.*, 2010]. It was suggested that the conics appear due to the adiabatic mirroring of the strahl population at *B* field enhancements inside the SIRs. The backstreaming, sunward propagating electrons were explained in terms of their energization at the SIR bounding shocks and compression waves and the subsequent leakage from the SIRs into the upstream region. Due to the way the IMF lines connect to the leading and trailing portions of the SIRs, the electrons streaming away from these structures always propagate sunward. The fluxes of these backstreaming populations may exceed those of the antisunward propagating strahl.

Suprathermal conics inside ICMEs were first reported by Feldman *et al.* [1999] and were suggested to originate in transient heating of electrons due to magnetic reconnection within magnetic legs of the coronal mass ejections (CMEs). Gosling *et al.* [2002] observed symmetric 90° PA depletions and conics in ICMEs and explained them in terms of double magnetic connection to the Sun and adiabatic motion of electrons.

Feldman *et al.* [1983b] performed a systematic study of electron VDFs at IP shocks. It was found that at weak shocks ($n_{\text{downstream}} / n_{\text{upstream}} \lesssim 2$ and $v_{\text{downstream}} - v_{\text{upstream}} \lesssim 70 \text{ km s}^{-1}$) the heating of the electrons is predominantly in the direction perpendicular to the *B* field, while for the strong shocks ($n_{\text{downstream}} / n_{\text{upstream}} \gtrsim 2$ and $v_{\text{downstream}} - v_{\text{upstream}} \gtrsim 70 \text{ km s}^{-1}$) it is predominantly in the direction parallel to the *B* field. In the latter case the stronger parallel heating is partly due to the acceleration by the stronger cross-shock potential. The downstream distributions at strong shocks develop a flattop and are

similar to distributions observed downstream of the Earth's bow shock. Suprathermal electron distributions similar to those described in the previous paragraphs were also observed at reverse shocks in the solar wind [Skoug *et al.*, 2006].

1.3. Ninety Degrees PA Enhancements

In this report we present another type of suprathermal electron pitch angle distributions (PADs), the 90° PA enhancements or ring distribution (we will use both terms in the text). These appear as enhanced phase space density (f_{dist}) values centered at 90° ± 10° PA. We find them in association with IP shocks. They can be the dominant population, much stronger than the strahl, or they can appear as fairly weak humps.

In the past such enhancements have been reported in the literature, but they were not studied specifically. *Feldman et al.* [1983b], *Hull et al.* [2001], and *Kajdič et al.* [2013] observed them just downstream of IP shocks. They explain the origin of these enhancements either in terms of strong perpendicular heating at shocks [*Feldman et al.*, 1983b] or due to the motion of electrons at supercritical shocks with magnetic overshoot [*Hull et al.*, 2001]. *Feldman et al.* [1999] show ring distributions in their Figure 3.5 that were observed inside an ICME and were attributed to electron heating due to newly reconnected field lines within the magnetic legs of the CMEs. The 90° PA enhancements also appear in Figure 1 of *Skoug et al.* [2006] but are not discussed in the paper.

The purpose of this paper is to study possible mechanisms responsible for the 90° suprathermal electron PA enhancements which are shown to be a frequent feature of suprathermal electrons in the vicinity of IP shocks. In section 2 we present our observations. First, we describe three case studies. Next we discuss the correlations between the presence of ring distributions and the statistical properties of IP shock. Finally, we look at the wave activity associated to these shocks and try to establish the link between the presence of the waves, their observational properties, and the ring distributions. In section 3 we discuss the observations, and in section 4 we draw conclusions.

2. Observations

For the purpose of this study we analyze time intervals ±1 h of the 232 IP shocks that were observed with the two STEREO spacecraft. We use the magnetic field and electron data provided by the IMPACT MAG and Solar Wind Electron Analyzer (SWEA) instruments [*Luhmann et al.*, 2008a, 2008b; *Sauvaud et al.*, 2008; *Acuña et al.*, 2008], respectively, STEREO/WAVES data for the study of plasma waves [*Bougeret et al.*, 2008], and the Plasma and Suprathermal Ion Composition (PLASTIC) data for ions [*Galvin et al.*, 2008].

The B field data are available in three modes—in the continuous modes with 1 Hz and 8 Hz time resolutions and in the burst mode with 32 Hz resolution.

The SWEA instruments were designed to provide measurements of SW electron distribution functions in the energy range between 1 eV and 2 keV in a 120° × 360° solid angle sector. The distribution functions are obtained every 2 s and are available in two different time resolutions, depending on the SWEA operational mode. Before 16 April 2009 the data had 30 s time resolution in a continuous operational mode and 2 s resolution in the burst mode. After that date, the continuous mode data have time resolution of 20 s, while the burst mode data have 4 s time resolution. Although the SWEA instrument was designed to also observe low-energy electrons, unexpected charging issues prevent it from obtaining reliable data for electrons with energies below 45 eV [see *Fedorov et al.*, 2011]. Hence, the core population of the solar wind electrons is not observed, but the suprathermal electron data are not affected. The PADs used in this paper have been calculated in the plasma frame of reference (as opposed to spacecraft frame) using ion speed data.

The STEREO/WAVES or S/WAVES consists of several instruments, among them the Time Domain Sampler (TDS). TDS is composed of three monopole electric antennas E_x , E_y , and E_z . It is intended to measure bursty, high-amplitude events, such as Langmuir waves, at high time resolution (250,000 samples/s in nominal mode). Although it measures many events, only the ones with the highest amplitudes (approximately 50 events/d) are transmitted to Earth.

The Langmuir Wave Statistics (LWS) is a TDS subsystem. It stores the highest amplitudes detected by each antenna during 40 ms time periods. It then makes statistics of these amplitudes by using 15,000 values obtained during consecutive 10 min periods. There are 144 of these statistics, or histograms, per day.

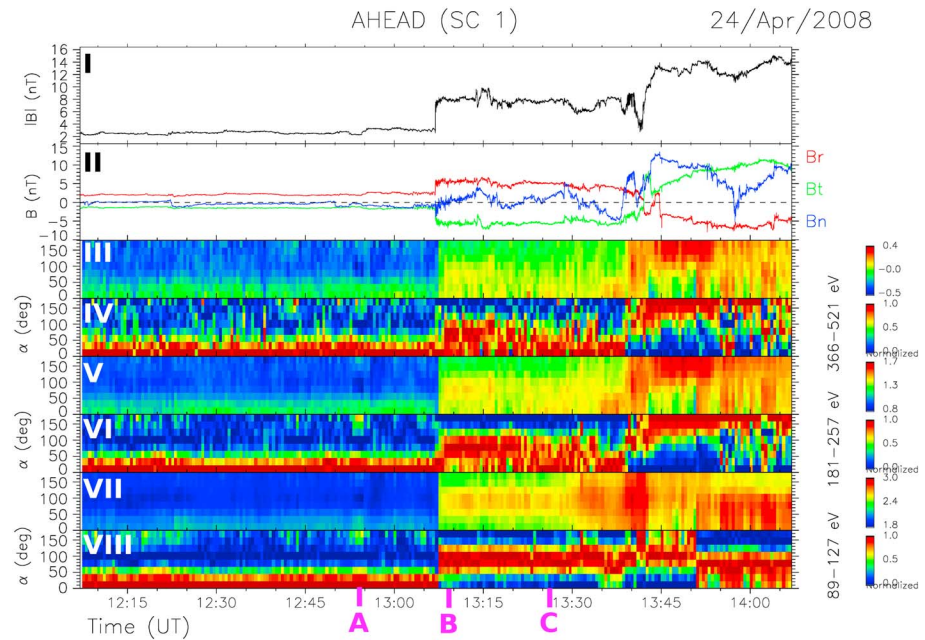


Figure 1. The 24 April 2008 shock. Plots show B field magnitude in units of nanotesla (nT) (I), B field components in nT (II), and pitch angle distributions (III–VIII). Three energy channels with central energies 400.6 eV, 246.6 eV, and 93.5 eV are shown. Plots III, V, and VII show color-coded logarithm of f_{dist} , while plots IV, VI, and VIII show normalized f_{dist} .

The data in each histogram are binned in 256 voltage intervals. Although the time resolution of LWS data is not very high, the advantage of using the data is that it is continuous.

The PLASTIC instrument provides solar wind ion distributions and moments with 1 min time resolution.

2.1. Case Studies

We show three case studies where 90° suprathermal electron PA enhancements appear adjacent to shock transitions.

2.1.1. The 24 April 2008 Shock

The first shock was observed on 24 April 2008 at 13:06:55 UT by the STEREO A spacecraft. This was an almost perpendicular SIR-driven forward shock with θ_{bn} (angle between the shock normal and the upstream IMF) equal to 82° . The shock's magnetosonic Mach number (M_{ms}) was 2.3, and its criticality ratio was $M_{\text{ms}} / M_c = 2.0$ (M_c is the first critical Mach number). The shock was of moderate strength with $B_{\text{down}} / B_{\text{up}} = 2.5$, and the upstream plasma beta (ratio of the thermal and magnetic pressures) was 4.1. During the time when the shock was observed, the spacecraft was operating in a normal mode, so the resolution of the SWEA data was 30 s. The shock is presented in Figure 1. On the panels we show the following: (I) magnetic field magnitude in units of nanotesla (nT) and (II) magnetic field components in the RTN coordinate system in nT. RTN is a spacecraft-centered coordinate system with \vec{R} being a Sun to spacecraft pointing vector, \vec{T} points in the direction of the cross product of \vec{R} with the Sun's spin axis, and \vec{N} completes the right-hand triad. Panels from (III) to (VIII) show the suprathermal electron pitch angle distributions (PADs) in the solar wind reference frame. Three energy channels with energy ranges 366–521 eV, 181–257 eV, and 89–127 eV are shown. Each channel is presented twice. The panels (III), (V), and (VII) show color-coded logarithm of the electron distribution function (f_{dist}) in units of $\text{km}^{-6} \text{s}^{-3}$. The panels (IV), (VI), and (VIII) show the normalized f_{dist} , calculated as $(f_{\text{dist}}(t) - f_{\text{dist,min}}(t)) / (f_{\text{dist,max}}(t) - f_{\text{dist,min}}(t))$ for each time sample. At a given time and energy $f_{\text{dist,min}}$ and $f_{\text{dist,max}}$ are respectively the minimum and maximum f_{dist} values.

We see that upstream of the shock the PADs show a continuous red or green trace at 0° PA, which is the solar wind strahl. Normalized panels reveal a weaker electron beam at 180° PA, which appears as an intermittent green trace. The purple lines at the bottom of the figure mark the times of the PADs shown in Figure 2. Figure 2a exhibits PAD upstream of the shock, while Figures 2b and 2c show downstream distributions.

The 90° enhancements appear immediately after the shock transitions. They are most obvious in Figure 1 in panels VII and VIII as a yellow and red trace at perpendicular pitch angles. This population is present

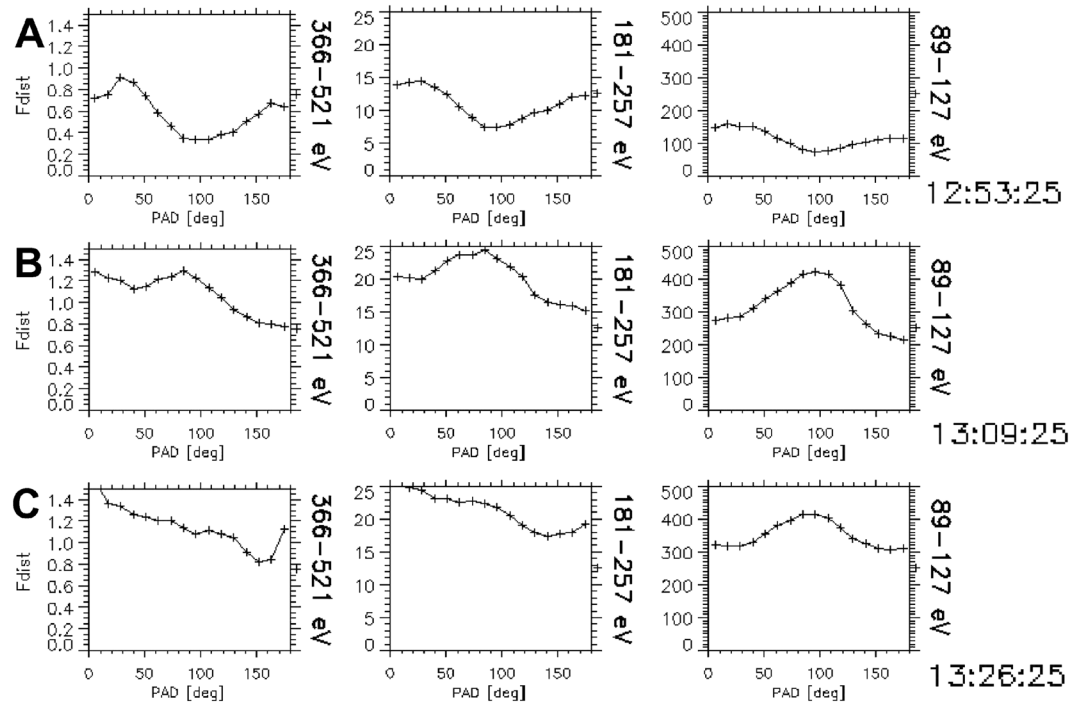


Figure 2. PADs at different times marked in Figure 1 with purple vertical lines.

until 15:03:55 UT, so for 2 h. In higher energy channels the distribution is not so apparent, but a careful examination reveals its presence. Also, in this case the population persists for a much shorter time period.

In Figure 2 we can see that the 90° enhancements can be the dominant population downstream of the shock in all three energy channels (Figure 2b). In Figure 2c we can see that this population has disappeared in the highest energy channel and that it is barely present in the 181–257 eV channel but that it is still the strongest at lowest energies. In some cases the f_{dist} values at 0° and 180° PA are almost the same upstream and downstream from the shock (see, for example, the middle column in Figure 4) which means that the 90° population was added to the already existing electron distribution.

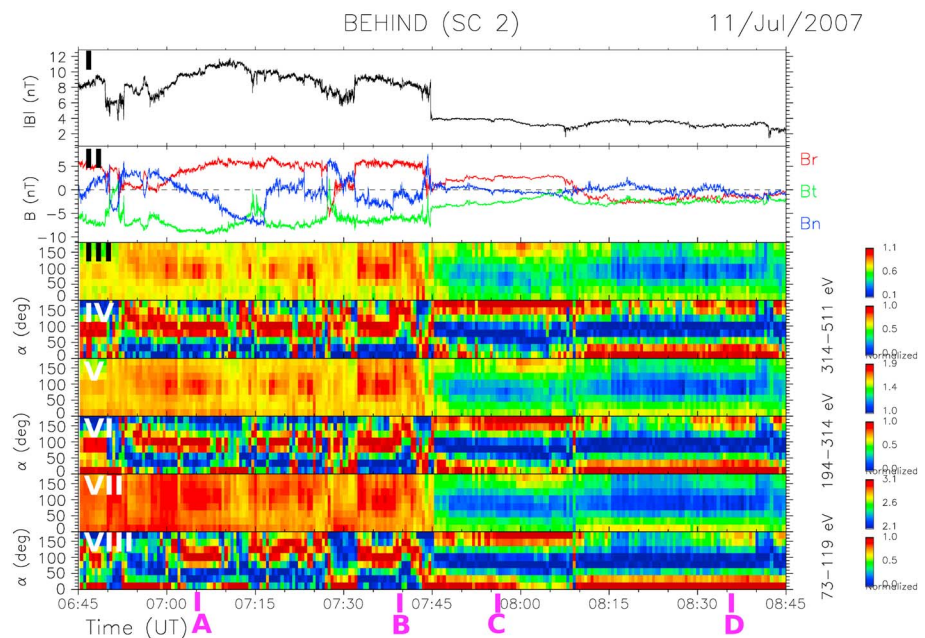


Figure 3. The 11 July 2007 shock. The format is the same as in Figure 1.

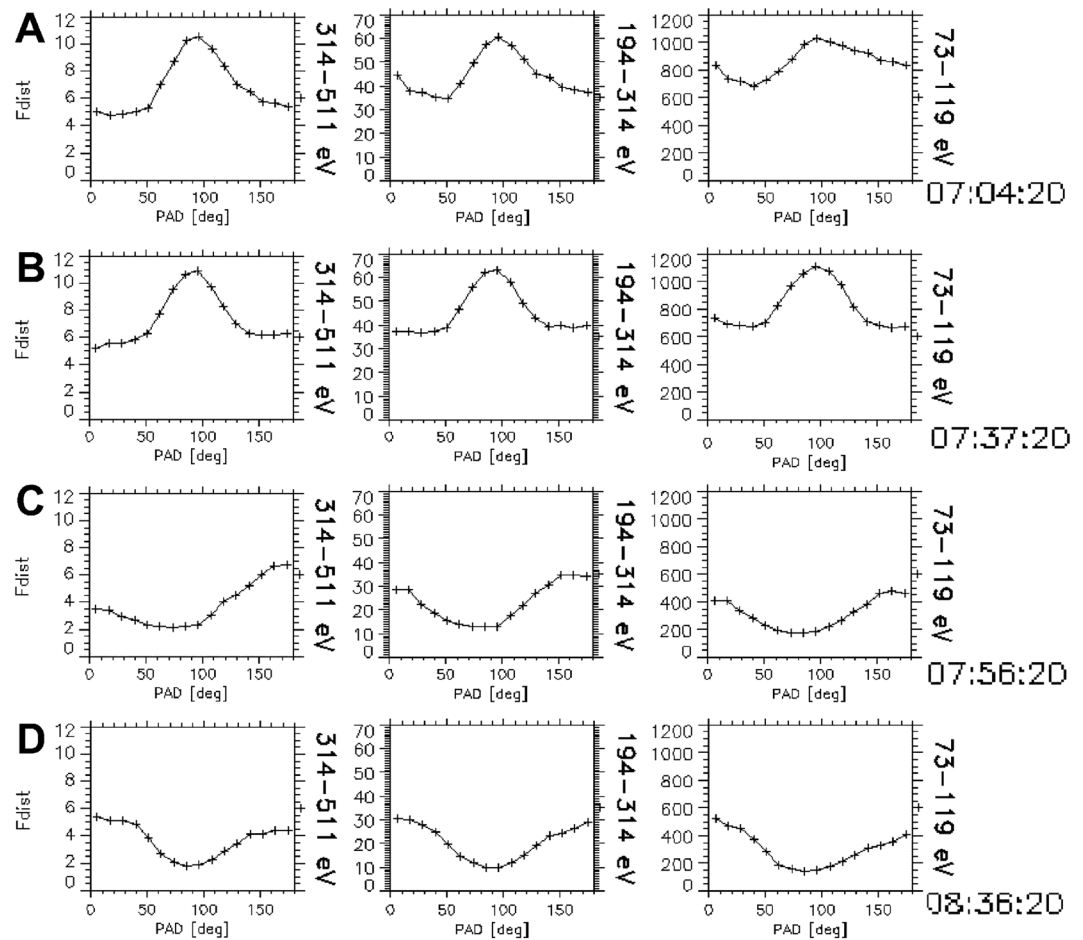


Figure 4. PADs at 11 July 2007 shock. The times of distributions are marked in Figure 3.

2.1.2. The 11 July 2007 Shock

This shock was observed on 11 July 2007 at 07:44:44 UT by the STEREO B spacecraft. It was a SIR-driven reverse shock of moderate strength ($B_{down}/B_{up} = 2.0$) and M_{ms} (1.8). It was marginally critical with a criticality ratio of 1.1 and quasi-perpendicular with $\theta_{Bn} = 63^\circ$. The plasma beta upstream was 0.94. The shock is presented in Figure 3 which has the same format as Figure 1.

Again, we see strong counterstreaming populations upstream of the shock, with the 0° and 180° PA strahls of similar strengths (also see Figure 4). Just downstream of the shock transition we see intermittent 90° enhancements in all three energy channels. This population persists from 05:56:46 UT, so during somewhat less than 2 h. This time the 90° PA enhancements appear equally persistent in all three energy channels and are by far the most dominant feature in the downstream region (see Figures 4a and 4b). Again, examining the f_{dist} values at 0° and 180° PA we see that these do not vary much from Figures 4a–4d.

2.1.3. The 9 June 2007 Shock

The 9 June 2007 shock was a SIR-driven forward shock (Figure 5) detected by STEREO A at 13:15:50 UT. It was a weak shock with $B_{down}/B_{up} = 1.3$ and $M_{ms} = 1.2$. It was supercritical with its $M_{ms}/M_c = 2.0$ and quasi-perpendicular ($\theta_{Bn} = 67^\circ$). This is one of the 11 shocks in our sample where we found 90° PA enhancements in its upstream region. Figures 5 and 6 show a strong 90° population in the lowest energy channel. This population appears upstream of the shock at 12:39:03 UT and continues downstream until 14:17:03 UT, so during 1 h and 40 min. The f_{dist} of this population can in some cases reach higher values than that of the strahl population located at 180° PA.

2.2. Statistical Properties of IP Shocks

The two STEREO spacecraft observed 236 IP shocks during the period 2007–2011. This period coincides with the last solar minimum and the rising phase of the solar cycle 24. The complete list of the IP shocks observed

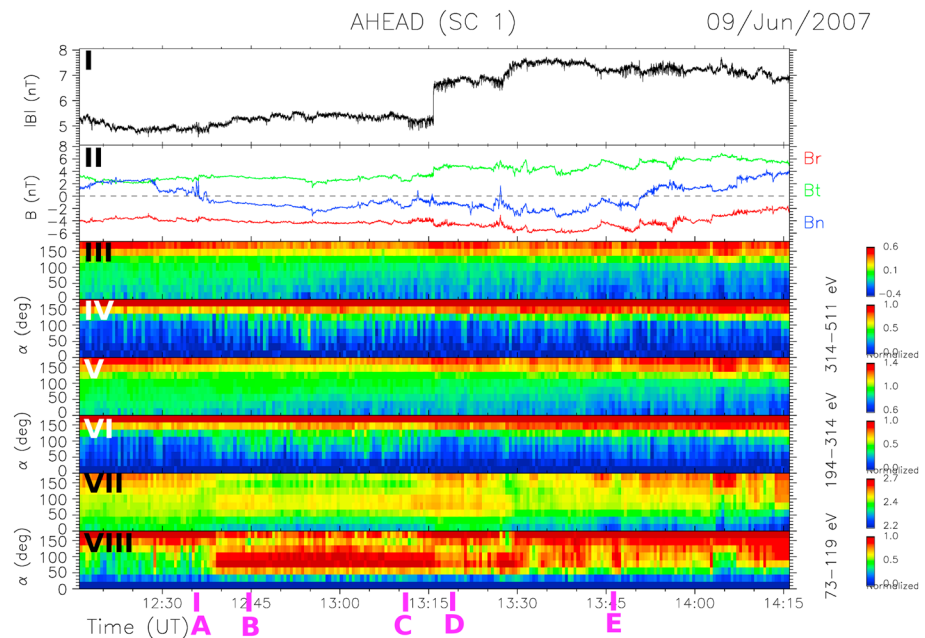


Figure 5. The 9 June 2007 shock. The format is the same as in Figure 1.

by STEREO can be found on the Institute of Geophysics and Planetary Physics web page http://www-ssc.igpp.ucla.edu/forms/stereo/stereo_level_3.html, and the selection criteria are described in *Jian et al.* [2013]. Plasma data are not available for the first four shocks observed in 2007, so only 232 are included in our study. The majority of them (167, 72%) were forward shocks while some (65, 28%) were reverse shocks. We identified 46 shocks to be driven by ICMEs and 132 by SIRs. Fifty-three shocks were either driven by complex events (consequence of interaction of two ICMEs, of an ICME and a SIR, or of an ICME and a fast stream) or we could not determine the driver (see also *Jian et al.* [2013]).

The observed shocks are fairly weak. Their strengths (the ratio of the downstream and upstream B field magnitudes) range from 1.03 to 2.91 with average value of 1.55 ± 0.30 . A large majority of the shocks (181, 78%) exhibited quasi-perpendicular geometry, while some (51, 22%) were quasi-parallel. The angles between the upstream IMF and the shock normals (θ_{Bn}) ranged from 11° to 89° with the average being $60^\circ \pm 17^\circ$. Their magnetosonic Mach numbers (M_{ms}) were quite modest, ranging from 1.07 to 4.05 with the average value of 1.55 ± 0.51 . We calculated the first critical Mach numbers at which shocks start reflecting ions (M_c) and found that 126 (54%) of them were supercritical (criticality ratio, $M_{ms} / M_c > 1$), while 106 (46%) were subcritical ($M_{ms} / M_c < 1$). The criticality ratios ranged from 0.5 to 3.7 with an average value of 1.16 ± 0.48 .

We survey time intervals starting 1 h upstream and ending 1 h downstream of the shocks to study the suprathermal electron PADs. In order for a distribution to be included in our sample we require that it exhibits a peak at $90^\circ \pm 10^\circ$ PA which must persist during at least three consecutive measurements. The latter requirement is used so as to exclude any false signals which could arise due to rapid fluctuations in the IMF and time aliasing of the PADs.

We observe the 90° PA enhancements in 114 (49.1%) cases. In 118 (50.9%) cases we did not find such distributions. The enhancements were detected starting immediately downstream of 52 (22.4%) shocks. Finally, we also observe them upstream of 11 shocks. Six of these 11 shocks exhibit the enhancements upstream and downstream of the shock transition, although they are not always continuous.

As a first step we compare statistical properties of shocks for which we do not observe the downstream 90° enhancements with those events where the enhancements are observed in the downstream region but not at the shock ramp (62 cases). These statistics are shown in Figure 7. In this figure we exhibit six histograms which show distributions of IP shocks according to the following: the shock strength (B_{down} / B_{up}), the angle between the upstream IMF and the local shock normal, θ_{Bn} , the radial (Sun-spacecraft) direction and the local shock normal, θ_{nx} , the plasma β , the magnetosonic Mach number, M_{ms} , and the criticality ratio, M_{ms} / M_c . The blue columns represent the shocks with no suprathermal electron 90° PA

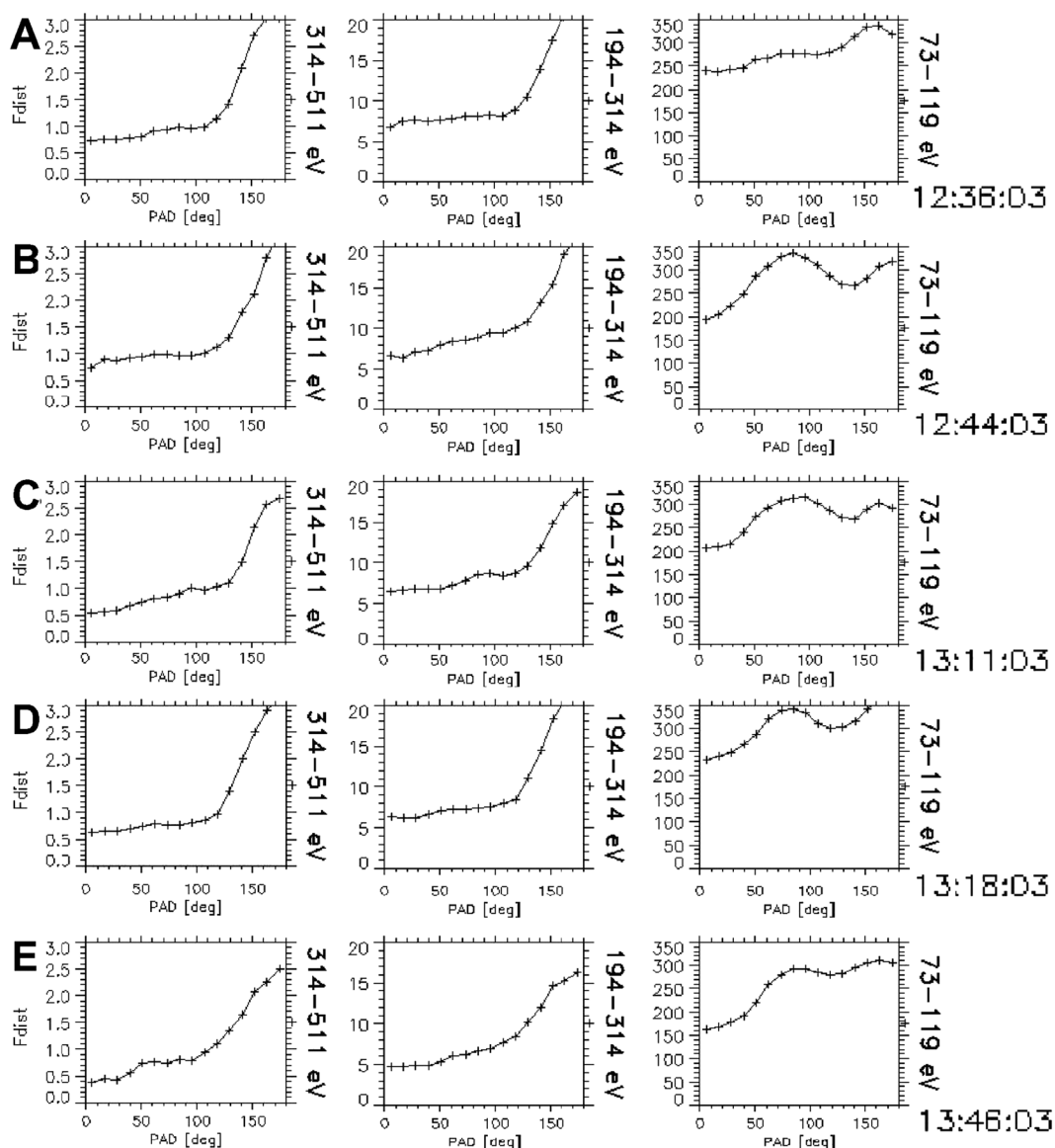


Figure 6. PADs at 9 June 2007 shock. The times of distributions are marked in Figure 5.

enhancements, while the black column represent those shocks at which these enhancements were detected in their downstream region away from the ramp. The average and median (μ) values and the standard errors of mean (σ) are also stated in each panel. These values will prove useful for later comparison of the properties of different shock populations. Vertical axes show the relative frequencies (ratios between the number of events in each bin and the total number of events).

We can see that statistical differences between the two samples are rather subtle. The shocks accompanied by the 90° enhancements are slightly stronger with $\langle B_{\text{down}} / B_{\text{up}} \rangle = 1.6$ versus 1.5 for shocks without the enhancements. The shocks with enhancements exhibit slightly higher magnetosonic Mach numbers ($\langle M_{\text{ms}} \rangle = 1.6$ versus 1.5) and tend to be somewhat more supercritical ($\langle M_{\text{ms}} \rangle / \langle M_c \rangle = 1.2$ versus 1.1) than the shocks at which these enhancements were not observed. Shocks with enhancements exhibit on average more perpendicular geometries with larger average θ_{Bn} (64° versus 55°) while their normals tend to be more aligned with the radial direction ($\langle \theta_{\text{nx}} \rangle$ values of 39° versus 46° for shocks without enhancements). The shocks without enhancements show a flatter θ_{Bn} distribution, while shocks with enhancements show a distributions that peaks for angles between 70° and 80° PA and with more than half of them having θ_{Bn} values between 60° and 80° PA. The average upstream solar wind β at shocks with 90° enhancements

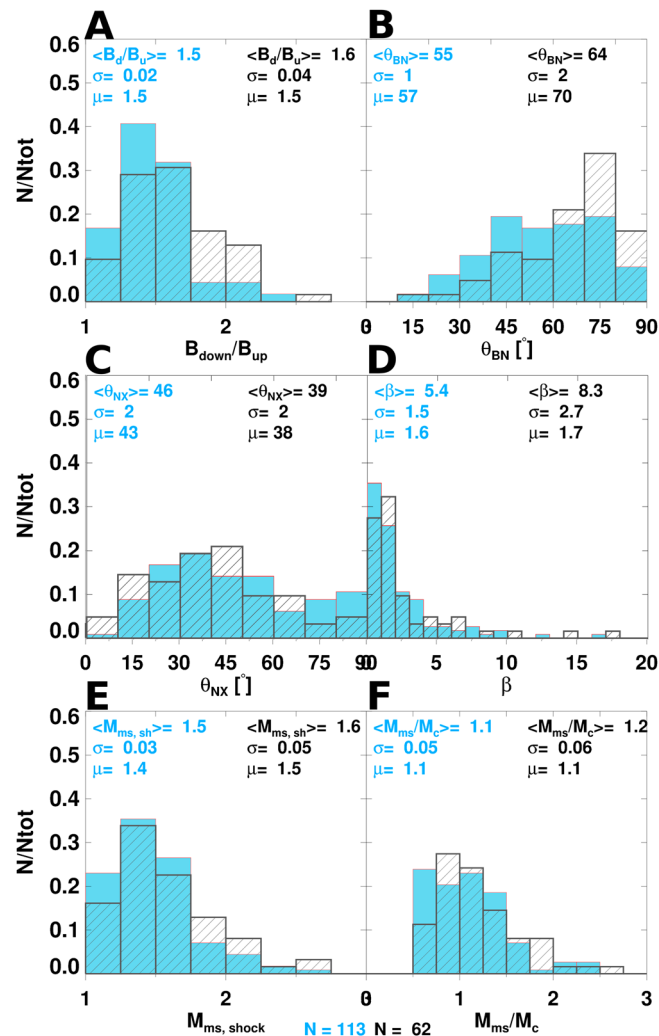


Figure 7. Statistical properties of IP shocks. Blue columns represent events with no ring distributions associated with them, while black, dashed columns represent shocks with downstream 90° enhancements. The latter were detected farther downstream of the shock transition. Different panels show distributions according to the following: (a) the ratio of downstream and upstream B field magnitudes (the shock strength, B_{down} / B_{up}), (b) the angle between the upstream IMF and the shock normal, θ_{Bn} , (c) the angle between the radial (Sun-spacecraft) direction and the shock normal, θ_{NX} , (d) upstream SW beta, (e) magnetosonic Mach number M_{ms} , and (f) criticality ratio (ratio between the magnetosonic Mach number and the first critical Mach number, M_{ms} / M_c).

observed in the vicinity of the shock transition. As before, the shocks with enhancements tend to be slightly stronger, more quasi-perpendicular, and with more radially oriented normals. Although on average the criticality ratio for both groups of shocks is the same, we can see that the distribution of the shocks with enhancements exhibits a strong peak for M_{ms}/M_c between 0.75 and 1. About 45% of the shocks in the group belong to this bin. For the shocks with enhancements the average value of upstream solar wind β is 1.9 while for the shocks without enhancements it is 5.4. The median values are much more similar, 1.6 and 1.8, respectively. We can see in the figure that there are shocks without enhancements with large values of β (between 5 and 12), while all the shocks with enhancements have β values less than 5.

Finally, in Figure 9 we show the comparison of properties of shocks with upstream 90° enhancements to those without enhancements. There were only 11 cases with upstream enhancements, so the statistics are not very significant. However, we can see that these shocks exhibit much more radially oriented normals

was 8.3, larger than upstream of shocks without enhancements (5.4). The shapes of the two distributions do not appear to be very different, so this difference is probably due to few very large betas upstream of shocks that exhibit 90° enhancements. The fact that their median values are very similar (1.6 and 1.7, respectively) supports this thesis.

We should mention that the θ_{Bn} were obtained from the coplanarity theorem. There is no other possibility since we only have measurements with one spacecraft, and not all velocity data are available. It was shown by several authors [e.g., Russell et al., 1983; Horbury et al., 2002] that this is not always a very reliable method for calculating the shock normals. In these two works the authors compared the normals of interplanetary shocks [Russell et al., 1983] and of the Earth's bow shock [Horbury et al., 2002] obtained from coplanarity theorem to those obtained from the four spacecraft measurements. The two sets of normals deviated in an important manner especially for very perpendicular shocks, where the difference in θ_{Bn} could be as large as 90°. Even for almost parallel shocks, the difference in θ_{Bn} was on the order of $\sim 10^\circ$.

In the next step we compare the properties of the shocks at which we found the 90° PA enhancements of suprathermal electrons starting just after the shock transition (52 cases) to those shocks that did not exhibit such enhancements (Figure 8). We do this because if the IP shocks produce the ring distributions, the properties of the latter will be less influenced by any spatial/temporal variations when

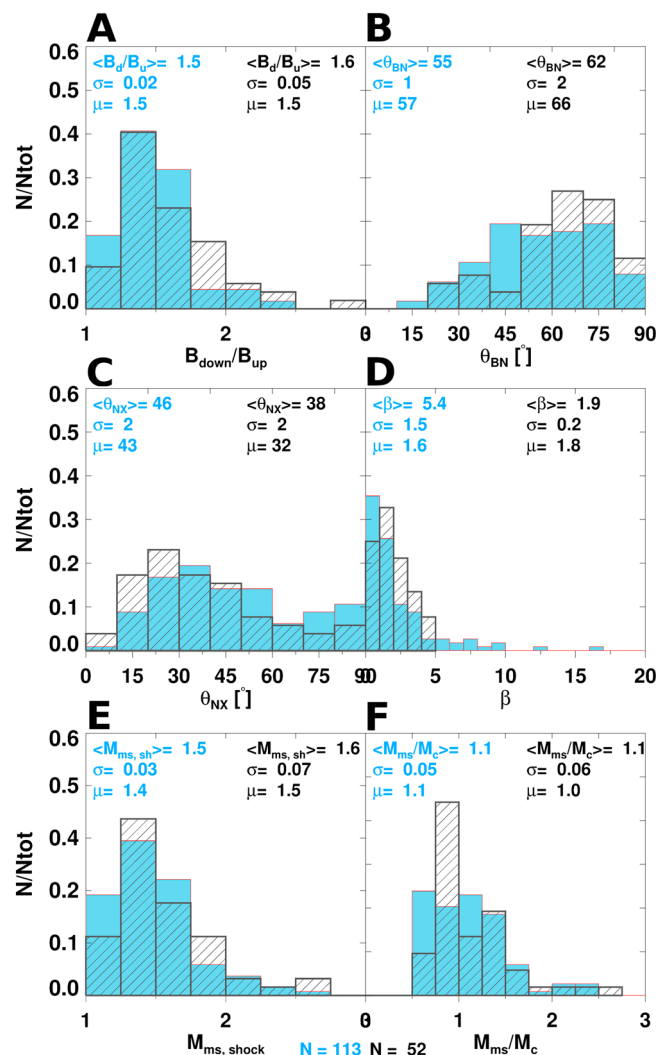


Figure 8. Statistical properties of IP shocks. The blue columns represent events with no associated ring distributions, while black, dashed columns represent those shocks where downstream 90° enhancements were detected just at the shock ramp. The format is the same as in Figure 7.

($\langle \theta_{NX} \rangle = 27^\circ$) than the other two groups of shocks. All but one shock are quasi-perpendicular. The average upstream β is 5.4, and the average θ_{BN} is 65° . Six out of 11 shocks exhibit criticality ratios between 0.75 and 1.

2.3. Wave Activity

In this section we study wave activity associated to IP shocks. We use the STEREO/WAVES (S/WAVES) data. We study the time intervals of 1 h before and after the shock transition.

S/WAVES measurements of plasma waves are strongly affected by high-rate impacts of interplanetary nanodust on the spacecraft [Zaslavsky *et al.*, 2012]. Therefore, we limit our study of waves to 48 IP shocks observed by STEREO A during the year 2011, given that the observed nanodust impact rate is close to zero on STEREO A during this period. A summary of wave activity is provided in Table 1.

2.3.1. Time Domain Sampler Results

Whenever a TDS record of wave activity during the studied time intervals exists, we calculate the amplitude, the frequency, and the polarization of the fluctuations (the latter two properties are calculated in the spacecraft frame).

The number of wave samples associated with each shock varies from 0 to 47. In total we obtained 556 wave samples downstream of 48 shocks. Since there is only one shock with upstream 90° enhancements in this subset, we limit our discussion here to downstream waves.

In Figure 10a we plot wave amplitudes versus their frequencies. The wave properties were calculated throughout the entire time interval in the TDS sample. Each symbol in this figure represents one wave sample. Different colors represent different cases of shocks to which the waves are associated: black asterisks are for the waves detected around shocks that do not exhibit 90° PA enhancements (19 shocks, 86 wave samples), the purple color stands for waves at shocks with enhancements starting immediately downstream of the shock transition (10 shocks, 184 samples), and the red asterisks are for shocks with enhancements farther downstream (19 shocks, 239 samples).

It seems as if the waves group into two subsets: the lower frequency fluctuations (0.01 kHz–0.2 kHz) tend to have lower amplitudes (2 mV/m–20 mV/m). This is especially true for the waves observed at shocks with ring distributions immediately downstream of IP shocks (purple asterisks) which seem to be confined to amplitudes of less than 9 mV/m. The higher-frequency waves (0.2 kHz–10 kHz), in general, exhibit higher amplitudes (5 mV/m–80 mV/m). Those higher-frequency waves that were observed at IP shocks that were not associated to ring distributions (black asterisks) all exhibit amplitudes larger than 10 mV/m. We should mention that there were few signals with amplitudes larger than 80 mV/m but were discarded, since they were probably produced by impacts of dust particles.

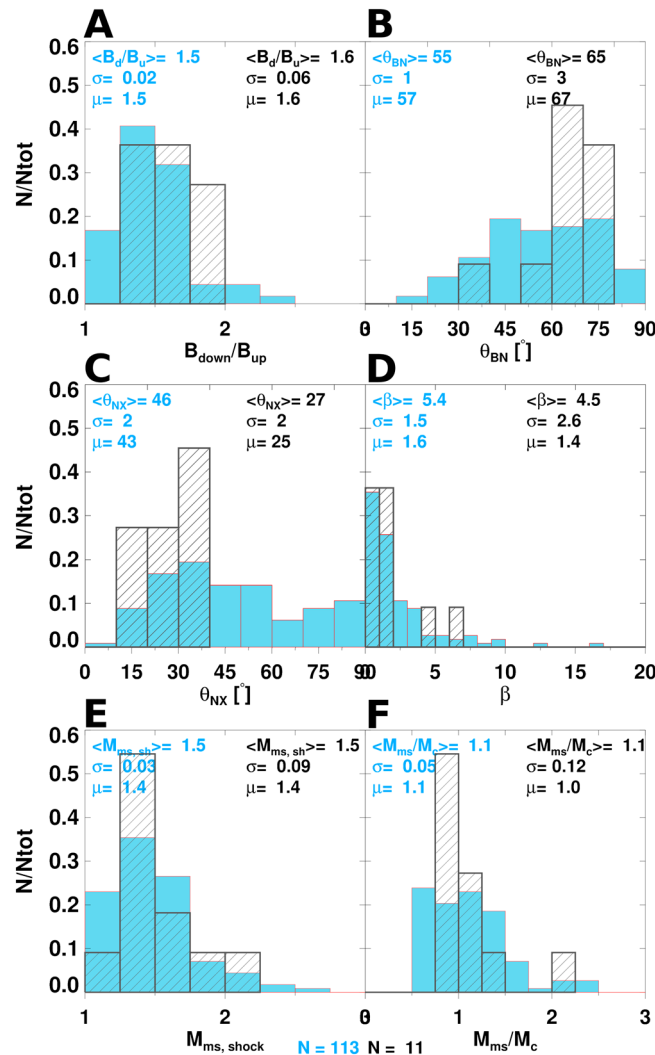


Figure 9. (a–f) Statistical properties of IP shocks. The blue columns represent events with no associated ring distributions, while black, dashed columns represent those shocks where upstream 90° enhancements were observed. The format is the same as in Figure 7. In one case the β value in front of the shock with upstream ring distribution was 29, and it is not shown on Figure 9d.

Figure 10b plots a proxy for polarization of the waves against their frequencies. This proxy is calculated as the ratio of the intermediate to the maximum eigenvalues which are derived from the minimum variance analysis. Values close to 0 mean linearly polarized fluctuations. When the proxy values are close to 1, the wave energy exhibits more or less equal repartition in at least two directions. These values are then compatible not only with circularly polarized waves but also with a random polarization. After performing a phase analysis on several of these waves we decided to treat them as circularly polarized.

The most common polarization measures of the lower frequency waves are between $\sim 7 \times 10^{-3}$ and $\sim 2 \times 10^{-1}$ regardless of if and where the ring distributions of suprathermal electrons were detected. The polarization measures of higher-frequency fluctuations tend to have values between $\sim 3 \times 10^{-2}$ and 1 if they were detected at shocks with 90° PA distributions immediately behind the shock (purple asterisks). If they were detected at shocks without the ring distributions (black) they cluster mostly between 10^{-2} and 4×10^{-2} . Those high-frequency fluctuations associated with IP shocks where suprathermal electron ring distributions were detected away from the shock transition (red) exhibit polarization measures in the range between 5×10^{-3} and 1.

On average the S/WAVES instrument sent 4.5 downstream wave samples per shock associated to events without 90° enhancements while these statistics are much higher when ring distributions were observed in the shocks' downstream regions (12.5 samples per shock) and when they were observed starting just at the shock transition (18.3 samples per shock). Here we remind the reader that S/WAVES transmits only a limited number of wave samples per day, so statistically more S/WAVES samples per unit time indicate more intense wave activity.

The higher-frequency fluctuations (>0.2 kHz) accounted for 35% of all fluctuations detected downstream of shocks with no ring distributions associated to them. In cases of shocks with downstream and immediate downstream distributions these percentages were 54% and 60%, respectively. Thus, higher-frequency fluctuations are more frequent at shocks associated with suprathermal electron ring distributions.

Figure 11 shows the wave distributions according to their (a and b) amplitude, (c and d) frequency, and (d and e) polarization. The logarithm of these quantities is presented on x axis. The bin widths are logarithmically spaced. In different columns we compare distributions for waves at shocks without 90° enhancements (blue bars) to other groups of shocks (black, dashed bars). In Figures 11a, 11c, and 11e the black bars

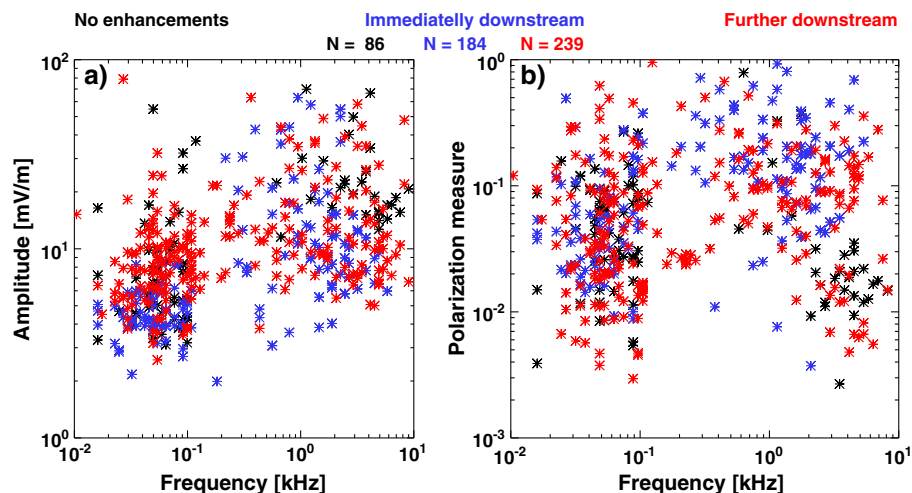


Figure 10. (a) Amplitude (in mV/m) and (b) polarization measure versus frequency (in kHz) of waves observed downstream of shocks with no associated 90° enhancements (black), with enhancements starting just at the shock ramp (purple) and farther downstream (red).

represent the waves observed at shocks with 90° enhancements just downstream of their ramps while in Figures 11b, 11d, and 11f they are for events at shocks with 90° enhancements farther downstream.

The amplitude distribution of waves at shocks without ring distributions (blue bars) is enhanced at amplitudes ≥ 16 mV/m (logarithmic value of 1.2) compared to the distribution of waves associated with ring distributions immediately at the shock ramp (Figure 11a). In Figure 11b we see that the waves detected farther downstream of the shock fronts exhibit narrower distribution than those not associated with ring distributions.

Figures 11c and 11d show distributions of waves according to their frequencies. It can immediately be seen that all three distributions seem to contain two populations: the first one is centered at lower frequencies around 40–50 Hz. The second population peaks at ~ 5 kHz for waves not associated with ring distributions or associated with ring distributions that appear farther downstream of the shocks. The distribution of higher-frequency waves observed at IP shocks with 90° PA enhancements just downstream of the shock ramp peaks at ~ 2 kHz.

Finally, Figures 11e and 11f exhibit the distributions according to the polarization. The polarization measure is defined so that zero values represent linearly polarized waves while values close to 1 are for circularly polarized fluctuations. We can see that the waves associated with ring distributions immediately behind the shock tend to be less linearly polarized than waves observed at with IP shocks with suprathermal electron enhancements farther downstream, which in turn tend to be slightly less linearly polarized than waves at shocks without the 90° PA enhancements.

Thus, we conclude that the wave activity tends to increase in association with 90° PA enhancements of suprathermal electrons and that these waves tend to be more elliptically polarized.

2.3.2. Langmuir Waves Statistics

Here we look at the Langmuir Wave Statistics (LWS) data set of the S/WAVES instrument.

Figure 12a shows LWS data during 7 October 2011. On that day STEREO A detected a forward shock at 17:15:24 UT and the downstream suprathermal electron ring distributions were observed starting just at the shock ramp.

Three different panels correspond to three different antennas, named X, Y, and Z. The amplitude is shown on the y axis in units of millivolts, while time is shown on the abscissa. The isocontours connect the points of equal number of samples in amplitude bins obtained at different times. There are three vertical lines—the middle one marks the time of the shock while the other two delineate the time interval ± 1 h of the shock. Intensity of the wave activity is presented as contours. The data consist of 144 statistics with 10 min time resolution, each containing 256 voltage intervals (see section 2 on LWS data).

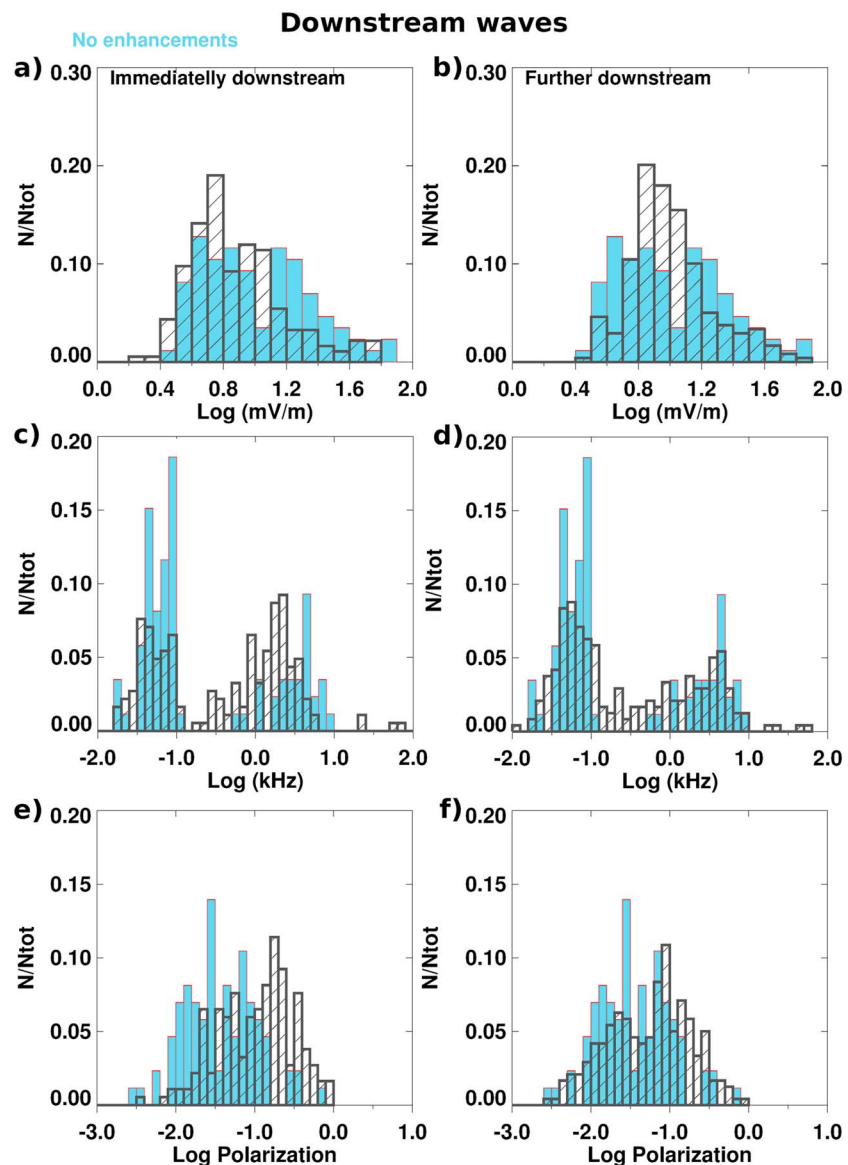


Figure 11. Distribution of properties of downstream waves ((a, b) amplitudes, (c, d) frequencies, and (e, f) polarizations) associated to shocks with no 90° PA enhancements (blue columns) and with shocks where the enhancements were detected immediately downstream of the shocks (black, dashed columns (Figures 11a, 11c, and 11e)) and farther downstream (black solid columns (Figures 11b, 11d, and 11f)). Logarithms of aforementioned quantities are given, and the bin widths are logarithmic.

We can see that during the whole day all three antennas show some wave activity at very low amplitudes $\lesssim 5$ mV, which corresponds to the noise. The noise at the Z antenna extends to higher voltages than the other two antennas. There are some time intervals when enhanced activity at higher voltages was detected (e.g., ~05:45 UT, ~06:15 UT, and ~12 UT). After the shock transition, in the shock sheath region, all three antennas detected enhanced wave activity compared to the preshock period.

The last two measurements before the shock transition begin at 17:00:00.6 UT and at 17:10:00.6 UT. During these two measurements all three antennas show a strong increase in wave activity up to voltages of ± 30 mV. The same is true for measurements centered at 16:20:00.6 UT and 16:30:00.6 UT, although the activity is somewhat less intense.

In Figure 12b we compare the signals of the antennas at times with and without electrostatic (ES) fluctuations. The continuous lines represent histograms of wave amplitudes at shock transition. Signals from three

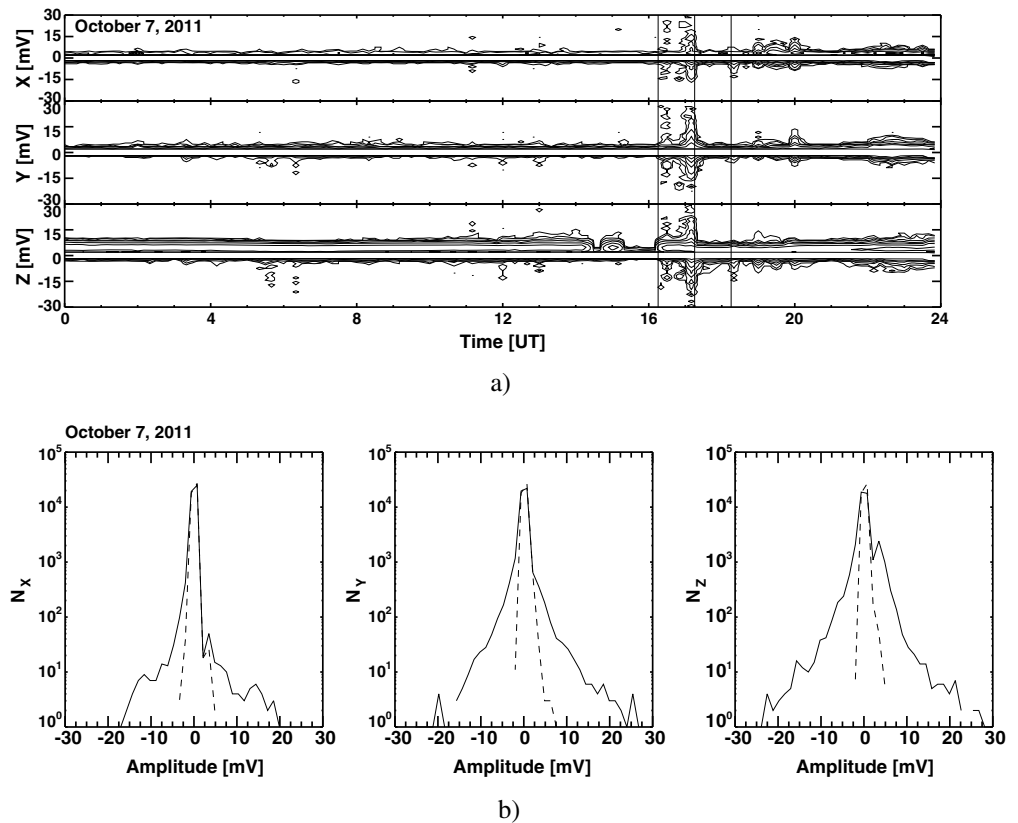


Figure 12. (a) Electrostatic fluctuation activity on 7 October 2011. The middle vertical line denotes the time of the shock, while the other two lines delimit the ± 1 h interval around the event. (b) Histograms made at time of the shock (black, continuous line) and at previous time, when only the noise was observed (dashed lines). The right, middle, and left panels correspond to the X, Y, and Z monopoles, respectively.

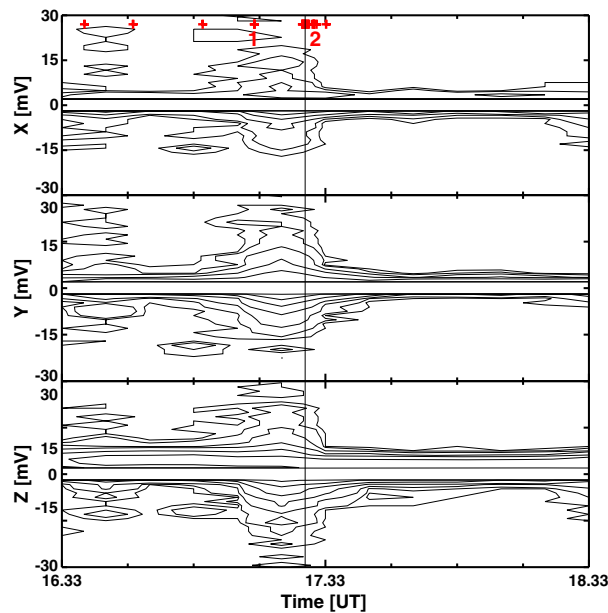


Figure 13. Electrostatic fluctuations near 7 October 2011 shock. Two hour time interval around the shock is presented here. Red crosses mark the times of wave samples provided by the TDS instrument. The vertical line marks the time of the shock.

measurements centered at 17:00:00.6 UT, 17:10:00.6 UT, and 17:20:00.6 UT were summed together. The dashed line shows a histogram with pure noise obtained between 1 and 2 h before the shock. We see that noise is present only at low amplitudes up to ~ 4 mV while, if present, at larger amplitudes the waves are the dominant source of the signal.

Figure 13 shows electrostatic activity during a 2 h time interval around 7 October 2011 shock. Red crosses mark the times of wave samples provided by the TDS instrument. The vertical line marks the time of the shock. In total, TDS provided 22 samples during this time interval (time between some of the wave samples is so short that the individual crosses cannot be distinguished in the figure). We present two of the wave samples in detail in Figures 14 and 15.

Figure 14 shows a sample of fluctuations of electric field observed 11 min and

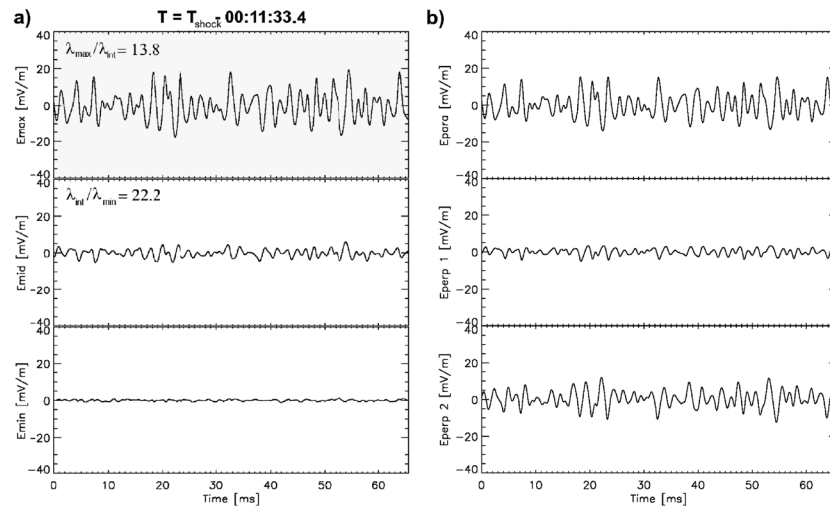


Figure 14. Fluctuations of electric field detected upstream of the 7 October 2011 shock. (a) The fluctuations in (from top to bottom) direction of maximum, intermediate, and minimum variance. (b) Fluctuations in the B field coordinate frame (see text for details).

33.4 s upstream of the shock (marked with number 1 in Figure 13). Figure 14a shows the fluctuations in the direction of their (from top to bottom) maximum (λ_{\max}), intermediate (λ_{int}), and minimum (λ_{\min}) variance. We can see on these panels that the ratio $\lambda_{\max}/\lambda_{\text{int}} = 13.8$ and $\lambda_{\text{int}}/\lambda_{\min} = 22.2$. This means that the waves are almost linearly polarized. Their frequency is ~ 0.33 kHz. Figure 14b shows the fluctuations in the B field frame of reference. The top plot exhibits them in the direction parallel to the magnetic field, while the other two plots show them in the directions perpendicular to it. The first perpendicular direction (Figure 14b (middle)) is defined as the vector product of the IMF direction with the x axis in the spacecraft coordinate system. Since this x axis approximately points radially to the Sun, and the IMF on average lies in the ecliptic plane, the first perpendicular-to-field axis points in a direction that is approximately perpendicular to the ecliptic plane. The second perpendicular-to-field direction (Figure 14b (bottom)) completes the right-hand system. We can see that the fluctuations have the smallest amplitudes in the direction that is approximately perpendicular to the ecliptic plane. Their amplitudes in the other two directions are almost the same, with the ones along the B field being larger.

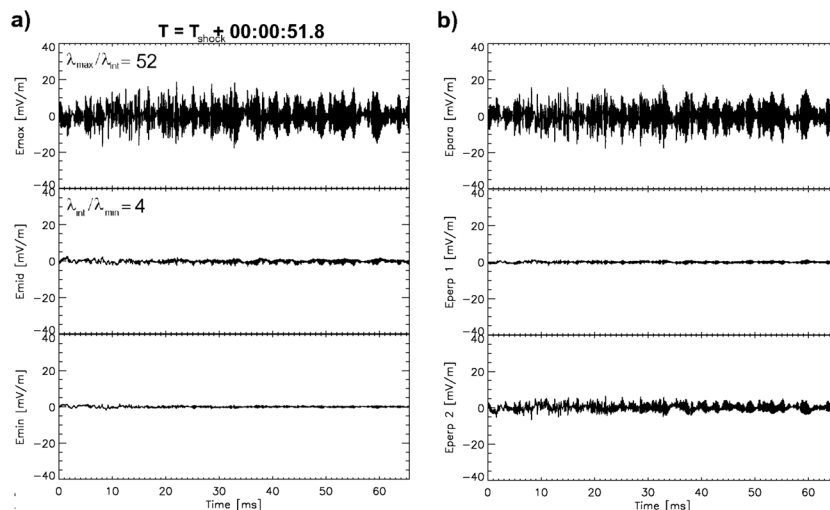


Figure 15. Fluctuations of electric field detected downstream of the 7 October 2011 shock. The format is the same as in Figure 14.

In Figure 15 we show another TDS sample observed 51.8 s after the shock (marked with number 2 in Figure 13). The format in this figure is the same as in Figure 14. Here $\lambda_{\max}/\lambda_{\text{int}}=52$ and $\lambda_{\text{int}}/\lambda_{\min}=4$ and the fluctuations are strongly linearly polarized in the direction parallel to the B field. Their frequency is ~ 5 kHz.

3. Discussion

In this report we study 90° PA enhancements of suprathermal electrons at IP shocks. We examine 2 h time intervals centered on the shock ramps. We find these enhancements at 114 out of 232 IP shocks observed with the STEREO spacecraft during the period 2007–2011. This is approximately half of the events which means that they are a common feature at IP shocks. In 52 (22.4%) cases we find ring distributions starting just downstream of the shock ramp.

In the first part of our research we try to determine whether the IP shocks at which ring distributions were detected in any way differ from the shocks that do not exhibit this feature. We compare shock properties, such as strengths normal orientation with respect to the upstream magnetic field and to the radial direction, upstream β , magnetosonic Mach numbers, and criticality ratio. We find that the differences are rather subtle if not insignificant. Probably, the main difference between the two groups of shocks is that those events that are associated with 90° enhancements tend to have larger θ_{Bn} angles. More than half of these shocks exhibit θ_{Bn} values between 60° and 80° . The same distribution of shocks without 90° enhancements is almost flat on the interval between $40^\circ < \theta_{\text{Bn}} < 80^\circ$. There are marginal differences in average values of shock strength, M_{ms} and criticality ratio.

We check for the possible correlation between the relative intensity of the 90° enhancements compared to the intensity of the halo, and the shock properties, such as their strength, M_{ms} , and criticality ratio (Figure 16). We define $\Delta f_{\text{dist,max}}$ at selected time and energy as the difference between the peak value of the suprathermal electron distribution function close to 90° PA which contains the contribution of the ring distributions ($f_{\text{dist,max}}$), to the value of the distribution function of the halo (f_{dist}). We find that the $\Delta f_{\text{dist,max}}/f_{\text{dist}}$ values range between 0.23 and 3.1. However, there is no correlation between these values and the shock properties. The latter is also true when we compare $f_{\text{dist,max}}$ values at 90° PA with the shock properties.

We also simulate the effect that crossing of an IP shock has on electron distribution function by performing Liouville mapping. We are especially interested in the role of the cross-shock potential. We do so by constructing the ad hoc electron distribution function composed of three components described by Maxwell velocity distribution functions (VDFs). These represent the isotropic core ($T = 10$ eV), halo ($T = 100$ eV), while we describe the strahl by a bi-Maxwellian VDF centered at parallel velocity equivalent to 35 eV and with parallel and perpendicular temperatures of 50 eV and 20 eV, respectively. Although *Maksimovic et al.* [2005] have shown that the halo component is best described by a bi-kappa distribution function, we use Maxwell distributions for all components for simplicity. This serves our purpose since we are only interested in qualitative behavior of the VDF at shock crossing. The total content of the strahl and the halo is about 10% of the core population.

Equations that relate the downstream pitch angles and velocities (α_2, v_2) to upstream values (α_1, v_1) in the solar wind reference frame are obtained by first taking into account the conservation of energy and magnetic momentum of electrons in the de Hoffman-Teller frame of reference:

$$E = \frac{1}{2} m_e v'^2 - e\phi^{\text{HT}} = \text{const}, \quad (1)$$

$$\mu = \frac{\frac{1}{2} m_e v'^2 \sin^2 \alpha'}{B} = \text{const}, \quad (2)$$

where v' , α' , ϕ^{HT} , and B are local values of electron velocity, pitch angle, cross-shock potential, and magnetic field, respectively; the electron mass is m_e .

After the transformation into the solar wind reference frame we obtain the following:

$$\tan \alpha_2 = \frac{v_1 \sin \alpha_1 \left(\frac{B_2}{B_1} \right)^{1/2}}{\sqrt{(v_1 \cos \alpha_1 + u_{\text{HT}})^2 + v_1^2 \sin^2 \alpha_1 \left(1 - \frac{B_2}{B_1} \right) - \frac{2e}{m} \Delta\phi - u_{\text{HT}}}}, \quad (3)$$

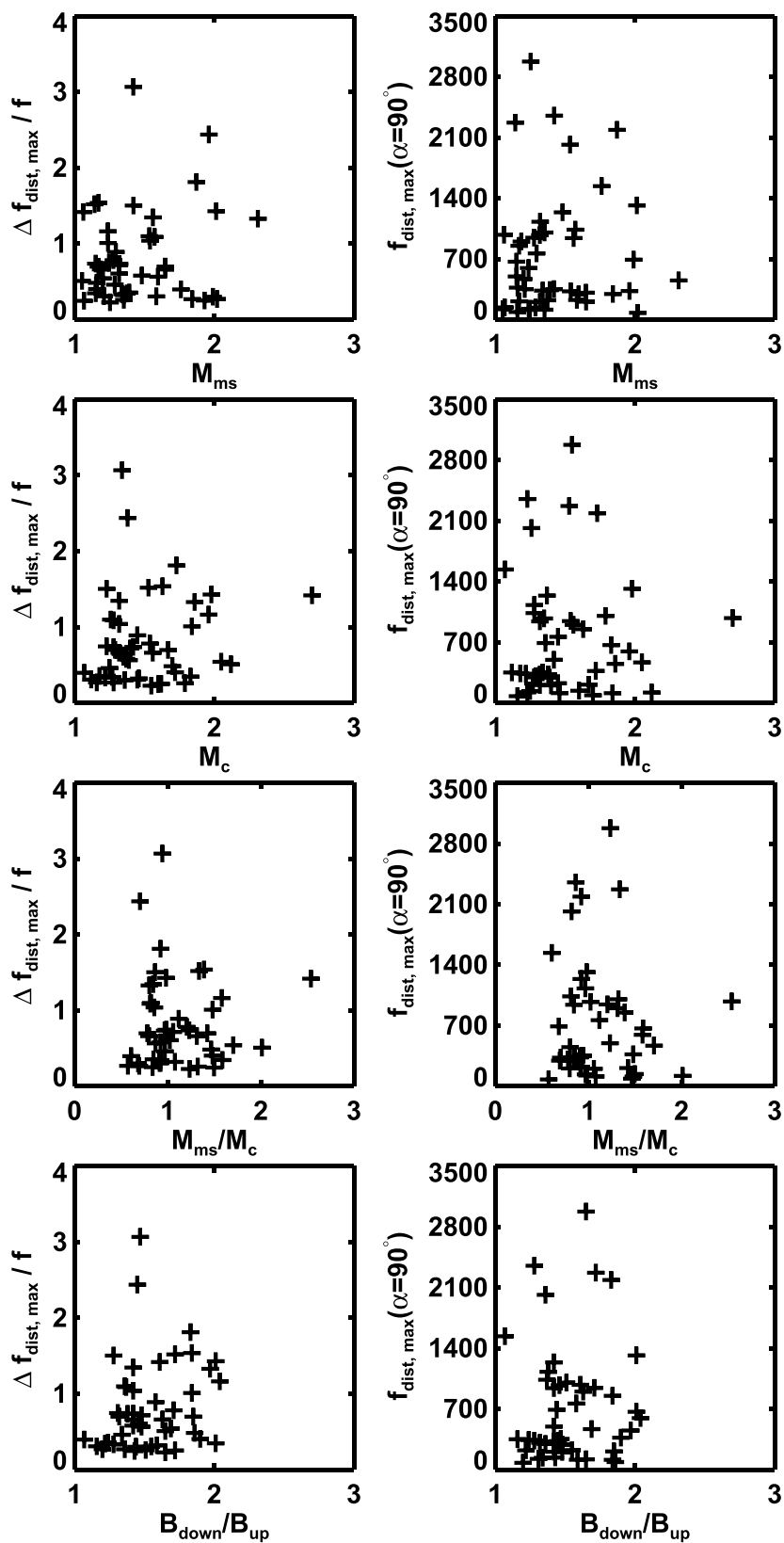


Figure 16. Maximum f_{dist} values of 90° PA enhancements versus four shock parameters: (top to bottom) magnetosonic Mach number, the first critical Mach number, criticality ratio, and shock strength. Relative enhancements ($\Delta f_{\text{dist,max}} / f_{\text{dist}}$) with respect to the halo values are shown on the left, while absolute values of maximum $f_{\text{dist,max}}$ are given on the right.

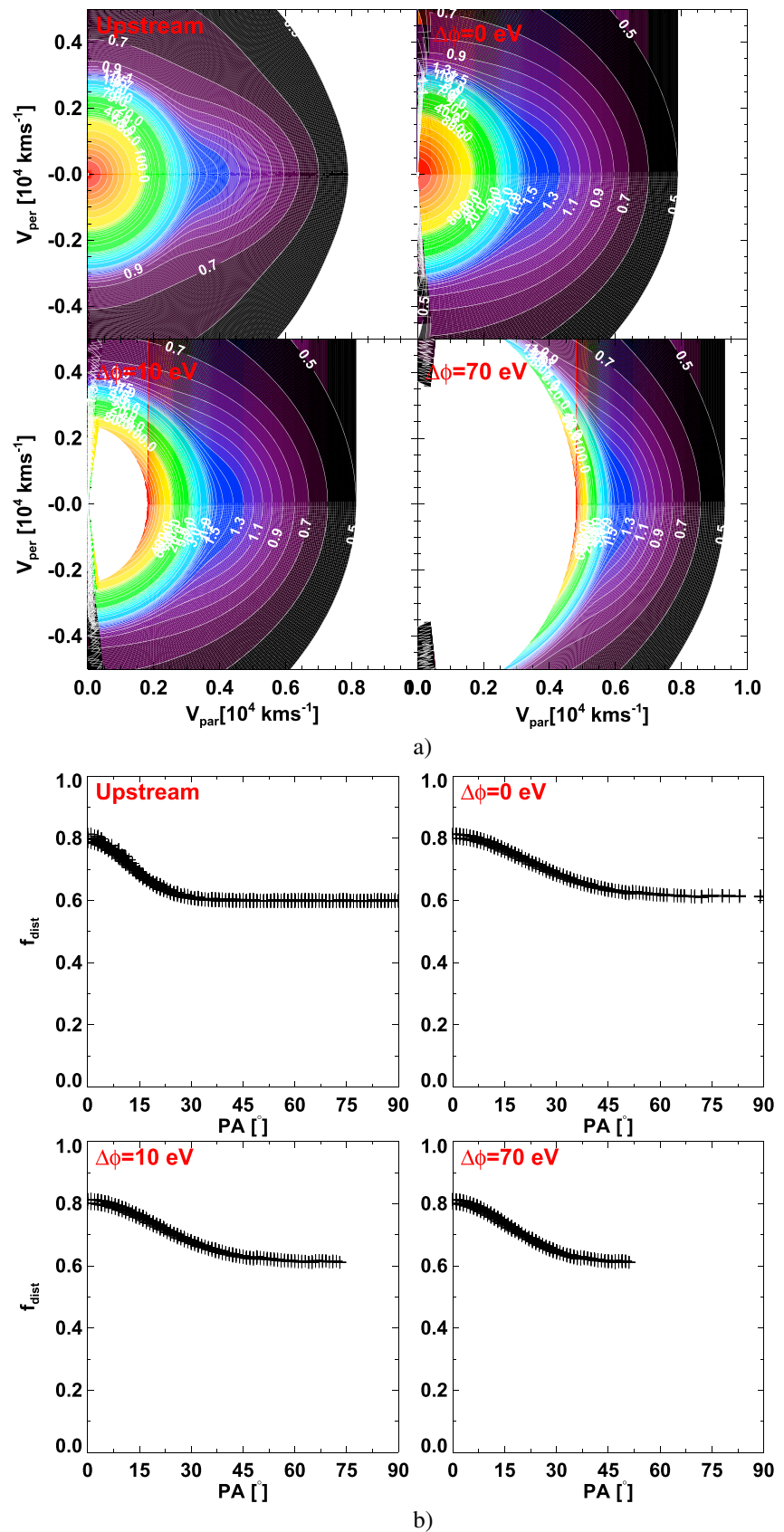


Figure 17

$$v_2 = v_1 \frac{\sin \alpha_1}{\sin \alpha_2} \left(\frac{B_2}{B_1} \right)^{1/2}. \quad (4)$$

Here B_1 and B_2 are the upstream and downstream magnetic fields, $\frac{2e}{m} \Delta \phi$ is the value of the cross-shock potential, and u_{HT} is the de Hoffman-Teller velocity in the solar wind rest frame and is calculated as follows:

$$\vec{u}_{\text{HT}} = \frac{\hat{n} \cdot \vec{u}}{\hat{n} \cdot \hat{b}} \cdot \hat{b}. \quad (5)$$

The shock normal is represented as \hat{n} , \hat{b} is the normal vector in the direction of the upstream magnetic field, and \vec{u} is the solar wind velocity vector in the shock rest frame. We calculate the u_{HT} to be 183 km s^{-1} in case of the 24 April 2008 shock, and this is the value used here.

The Liouville mapping is then performed by taking into account the following:

$$f_{\text{dist},1}(v_1, \alpha_1) = f_{\text{dist},2}(v_2(v_1, \alpha_1), \alpha_2(v_1, \alpha_1)). \quad (6)$$

We perform the Liouville mapping for cross-shock potential values of 0, 10, and 70 eV. The results are presented in Figure 17a. The isocontours on the plots represent the points of constant f_{dist} . The x axis is parallel to the magnetic field. The top left panel shows the upstream distribution, while the other panels exhibit the mapped distributions in the downstream region using the cross-shock potential values of 0, 10, and 70 eV. It can be seen that higher values of cross-shock potential lead to stronger acceleration of the electrons along the magnetic field. As the values of the cross-shock potential increase, the electron VDF becomes progressively more narrow in direction parallel to the B field while it broadens the perpendicular direction. The mapped distributions show some artifacts near $v_{\text{par}} = 0$, where the isocontours suddenly bend toward $v_{\text{par}} = 0$, indicating lower f_{dist} values there. Finally, Figure 17b shows pitch angle distributions for 100 eV electrons. Only the points with $\text{PA} \leq 90^\circ$ are shown. We can observe the widening of the strahl. However, we can see from both figures that the adiabatic motion with or without cross-shock potential cannot produce the ring distributions.

Another possibility to produce ring distributions is trapping of electrons between two magnetic mirrors. Trapping of electrons downstream of the Earth's bow shock has been invoked in the past in order to explain electron temperature anisotropies there. It was first noted by *Gosling et al.* [1989] that suprathermal electron distributions downstream of the Earth's bow shock become more anisotropic ($T_{\perp,e} > T_{\parallel,e}$) farther inside the magnetosheath. Later, *Masood and Schwartz* [2008] reported that just behind the Earth's bow shock $T_{\parallel,e} > T_{\perp,e}$, but farther in the magnetosheath the situation is reversed.

The latter could partly be explained by trapping of the electrons in the magnetosheath. IMF lines in the magnetosheath penetrate the bow shock twice. While electrons on these lines with PAs close to 0° and 180° can escape into the upstream region, the ones with large PAs cannot due to the cross-shock potential and so they are trapped in the magnetosheath.

Hull et al. [2001] have shown a similar effect at IP shocks. In this case the shock overshoot instead of the fore-shock potential was proposed to be responsible for trapping of the electrons near the shock front. However, in Figures 7 and 8 we can see that downstream 90° enhancements occur also at subcritical shocks, which do not have overshoots. We also visually inspected all the shock transitions and found some 90° enhancements at shocks that did not appear to have overshoots.

Masood and Schwartz [2008] state that in case of the Earth's bow shock, the adiabatic behavior alone cannot account for all of the observed perpendicular heating and that there must exist an additional, ongoing mechanism that continuously inflates the suprathermal electron population at perpendicular pitch angles. One of the possibilities mentioned by the authors is wave-particle interactions.

Figure 17. Liouville mapping. (a) A simulated upstream electron distribution (top, left). The rest of the panels exhibit downstream distributions where cross-shock potentials of 0, 10, and 70 eV were used. Red color indicates high values while blue and black colors indicate lower values of f_{dist} . (b) The four panels show PAD of electrons with $E = 100$ eV. Again, Figure 17b (top, left) is for the upstream distribution, while the other panels show downstream distributions with different cross-shock potentials. The f_{dist} units are arbitrary.

Table 1. Wave Activity at 48 IP Shocks Observed With STEREO A in 2011^a

Date	Time (UT)	Reverse/Forward	ES	ES at Shock	90° Enhancements	No. of Downstream TDS Samples
17/01/2011	18:31:00	R	y	y	Farther downstream	5
23/01/2011	17:06:06	F	y	n	Starting at shock ramp	7
25/01/2011	00:06:06	R	n	n	No	0
18/02/2011	17:43:43	F	y	y	Farther downstream	35
09/03/2011	06:47:47	F	n	?	No	8
19/03/2011	11:24:40	F	y	y	Farther downstream	14
22/03/2011	03:57:38	F	y	y	Farther downstream	7
22/03/2011	18:21:06	F	y	y	Farther downstream	18
31/03/2011	12:37:10	R	n	n	No	8
09/04/2011	13:39:33	R	n	n	No	1
11/04/2011	12:08:00	F	y	y	Farther downstream	13
22/04/2011	10:59:17	F	n	n	No	4
07/05/2011	11:32:53	R	y	?	Farther downstream	33
04/06/2011	18:48:50	R	y	y	Farther downstream	11
05/06/2011	18:59:01	F	y	y	No	12
09/06/2011	22:40:53	F	y	n	Farther downstream	22
16/06/2011	03:10:23	F	y	y	Starting at shock ramp	18
12/07/2011	03:47:04	F	y	n	Starting at shock ramp	33
23/07/2011	09:41:09	F	y	n	Starting at shock ramp	7
24/07/2011	22:36:05	R	y	n	No	16
06/08/2011	12:42:40	F	y	n	Farther downstream	11
11/08/2011	05:38:58	F	y	y	Farther downstream	16
13/08/2011	19:43:21	F	y	y	No	16
08/09/2011	16:01:27	F	y	y	Starting at shock ramp	17
11/09/2011	08:51:29	F	y	n	No	5
21/09/2011	22:35:45	F	y	n	No	2
24/09/2011	08:30:41	F	y	y	Farther downstream	45
28/09/2011	03:54:30	F	y	n	Starting at shock ramp	13
02/10/2011	06:53:15	F	n	n	No	2
03/10/2011	02:28:25	F	n	n	No	7
06/10/2011	03:55:07	F	y	n	Starting at shock ramp	4
07/10/2011	17:15:24	F	y	y	No	22
23/10/2011	20:59:00	F	y	y	No	7
25/10/2011	04:51:14	F	y	y	Farther downstream	20
05/11/2011	21:12:10	F	y	y	Farther downstream	13
06/11/2011	12:35:14	R	y	n?	No	2
20/11/2011	21:50:23	R	n	n	Starting at shock ramp	9
23/11/2011	17:35:05	R	y	y?	Farther downstream	18
25/11/2011	21:39:04	F	n	n	Upstream	14
26/11/2011	18:09:24	F	y	y	Starting at shock ramp	11
28/11/2011	14:51:26	F	y	y	Upstream and continues downstream	47
12/12/2011	03:47:21	R	n	n	No	13
17/12/2011	02:05:07	F	y	y	Farther downstream	34
21/12/2011	00:30:00	R	y	y	No	17
21/12/2011	09:27:28	F	y	y	No	16
28/12/2011	01:28:46	F	y	y	No	3
28/12/2011	20:47:09	R	y	y	Starting at shock ramp	11

^aThe columns contain dates and times of the shock observations, information on whether the events are forward or reverse shocks, on the presence of ES fluctuations during the time interval ± 1 h of the shock transition, on the presence of 90° enhancements, and on the number of downstream TDS samples sent by the S/WAVES instrument.

On the other side, *Michell et al.* [2012] show that the observed electron temperature just downstream of the Earth's bow shock is affected by electrons of different energies and pitch angles that have crossed the bow shock at different locations, making the bow shock heating a global problem. Other effects, such as wave-particle interactions, are expected to play a more important role deeper inside the magnetosheath.

Similar interactions have also been proposed to limit the perpendicular heating of the electron distribution function. *Gary et al.* [2005] predicted that electron anisotropies in the Earth's magnetosheath with $T_{\perp,e} > T_{\parallel,e}$ drive whistler anisotropy instability, which imposes the upper limit to the maximum $T_{\perp,e} / T_{\parallel,e}$ values.

From all this we would expect the electron anisotropies to be accompanied by electromagnetic wave activity. There is indication in STEREO data that 90° PA enhancements of suprathermal electrons and wave activity at IP shocks are associated.

The average number of TDAS samples of electric field fluctuations per shock is higher for shocks with downstream 90° PA enhancements (12.5 per shock) when compared to shocks without enhancements (4.3 per shock). It is even higher if those enhancements start just after the shock transition (18.5 per shock). The fluctuations observed by the TDAS mode seem to group into two populations: the lower frequency ($0.01 \text{ kHz} \lesssim f \lesssim 0.2 \text{ kHz}$) and the higher-frequency ($0.2 \text{ kHz} \lesssim f \lesssim 10 \text{ kHz}$) waves. Both frequency ranges are in the spacecraft frame. We can compare these frequencies to the typical electron gyrofrequency, f_e , and electron plasma frequency, f_{pe} , in the solar wind at 1 AU, which are $\sim 0.14 \text{ kHz}$ and $\sim 20 \text{ kHz}$, respectively. Similar feature in the spectra of electric and magnetic fluctuations in the vicinity of the IP shocks have long been known (see *Gurnett* [1985], for a nice review). The equivalent typical frequencies of the protons, f_p and f_{pp} , at 1 AU are $\sim 0.077 \text{ Hz}$ and $\sim 0.5 \text{ kHz}$. Although the unambiguous determination of the wave modes is beyond the scope of this paper, we can see that the lower frequency fluctuations in the range $f_p < f \lesssim f_e$ are consistent with either whistler waves or ion-acoustic waves [e.g., *Balikhin et al.*, 2005]. Some of the higher-frequency fluctuations are consistent with lower hybrid waves [e.g., *Walker et al.*, 2008].

From the LWS statistics we see that electrostatic fluctuations are present downstream of 90% of the shocks which also exhibit downstream 90° enhancements. For shocks without enhancements, this fraction is only 63%.

If a mechanism similar to the one proposed by *Masood and Schwartz* [2008] for the case of the Earth's magnetosheath does exist in the regions downstream of IP shocks, it must act more locally, since the ring distributions are not detected throughout the IP shock sheath regions.

4. Conclusions

Here we provide some conclusions that follow from our research:

1. The 90° PA enhancements of suprathermal electrons are a common feature downstream of IP shocks. We find them downstream from 114 (49%) of total 232 IP shocks.
2. Such enhancements also appear, although more rarely, upstream of the IP shocks. We find ring distributions upstream of 11 (4.7%) shocks.
3. There are no substantial statistical differences between the shocks that are associated with 90° PA enhancements and those that are not. The largest difference is in average θ_{Bn} , which is 64° for shocks associated with ring distributions and 55° for shocks that are not associated with them.
4. Electric field fluctuations in the radio part of the spectra seem to be enhanced at shocks associated to ring distributions—the number of waves samples sent by the TDS instrument was 4.5 per shock for events not associated with enhancements, and it was 18.3 samples/shock for events where the enhancements were detected starting just downstream of the shock ramp.
5. Electric field fluctuations at IP shocks can be divided into two groups depending on their frequencies. The lower frequency waves ($<0.2 \text{ kHz}$) tend to have lower amplitudes (between 2 mV/m and 20 mV/m) and exhibit polarizations uniformly distributed between linear and circular. Higher-frequency waves ($>0.2 \text{ kHz}$) tend to have higher amplitudes (5 mV/m–80 mV/m) and are slightly more elliptically polarized.
6. At shocks associated with 90° PA enhancements of suprathermal electrons, the higher-frequency waves account for 60% of all fluctuations. At shocks not associated with suprathermal electron PA enhancements of this proportion is 35%.
7. Of 29 shocks associated with downstream ring distributions (observed by STEREO A in 2011), 27 (93%) also exhibit downstream ES fluctuations. Of the 10 IP shocks that exhibit 90° PA enhancements starting just at the shock transition, 9 (90%) show enhanced downstream ES wave activity. ES fluctuations are also present at 12 (63%) IP shocks without suprathermal electron 90° PA enhancements.
8. Finally, we show that pure adiabatic effects at shock transition cannot fully account for the formation of 90° PA enhancements.

The definite origin of these suprathermal electron pitch angle enhancements remains unknown for now, and a more detailed study of the properties of electric and magnetic field fluctuations at IP shocks will be necessary in order to determine which mechanisms are responsible for their formation.

Acknowledgments

The authors acknowledge the CL/CLWeb team (<http://clweb.cesr.fr>). P.K.'s and A.O.'s work was possible due to an ESA research fellowship. The work at IRAP was supported by CNRS and CNES. L.K.J.'s and J.G.L.'s work is supported by NASA's Science Mission Directorate as part of the STEREO project, including the IMPACT and PLASTIC investigations. The French contribution to the S/WAVES investigation has been supported by both CNES and CNRS. X.B.C. is grateful for DGAPA grant PAPIIT IN105014. The authors also acknowledge Karim Meziane for useful discussions on Liouville mapping.

Yuming Wang thanks Ruth Skoug and another reviewer for their assistance in evaluating the paper.

References

- Acuña, M. H., D. Curtis, J. L. Scheifele, C. T. Russell, P. Schroeder, A. Szabo, and J. Luhmann (2008), The STEREO/IMPACT magnetic field experiment, *Space Sci. Rev.*, *136*, 203–266, doi:10.1007/s11214-007-9259-2.
- Anderson, B. R., R. M. Skoug, J. T. Steinberg, and D. J. McComas (2012), Variability of the solar wind suprathermal electron strahl, *J. Geophys. Res.*, *117*, A04107, doi:10.1029/2011JA017269.
- Balikhin, M., S. Walker, R. Treumann, H. Alleyne, V. Krasnoselskikh, M. Gedalin, M. Andre, M. Dunlop, and A. Fazakerley (2005), Ion sound wave packets at the quasiperpendicular shock front, *J. Geophys. Res.*, *32*, L24106, doi:10.1029/2005GL024660.
- Bougeret, J. L., et al. (2008), S/WAVES: The radio and plasma wave investigation on the STEREO mission, *Space Sci. Rev.*, *136*, 487–528, doi:10.1007/s11214-007-9298-8.
- Fairfield, D. H., and J. D. Scudder (1985), Polar rain: Solar coronal electrons in the Earth's magnetosphere, *J. Geophys. Res.*, *90*, 4055–4068.
- Fedorov, A., A. Opitz, J.-A. Sauvaud, J. G. Luhmann, D. W. Curtis, and D. E. Larson (2011), The IMPACT Solar Wind Electron Analyzer (SWEA): Reconstruction of the SWEA transmission function by numerical simulation and data analysis, *Space Sci. Rev.*, *161*, 49–62, doi:10.1007/s11214-011-9788-6.
- Feldman, W. C., J. R. Asbridge, S. J. Bame, M. D. Montgomery, and S. P. Gary (1975), Solar wind electrons, *J. Geophys. Res.*, *80*, 4181–4196.
- Feldman, W. C., J. R. Asbridge, S. J. Bame, J. T. Gosling, and D. S. Lemons (1978), Characteristic electron variations across simple high-speed solar wind streams, *J. Geophys. Res.*, *83*, 5285–5295.
- Feldman, W. C., S. J. Bame, S. P. Gary, J. T. Gosling, D. McComas, M. F. Thomsen, G. Paschmann, N. Schopke, M. M. Hoppe, and C. T. Russell (1982a), Electron heating within the Earth's bow shocks, *Phys. Rev. Lett.*, *49*, 199–201.
- Feldman, W. C., R. C. Anderson, J. R. Asbridge, S. J. Bame, J. T. Gosling, and R. D. Zwickl (1982b), Plasma electron signature of magnetic connection to the Earth's bow shock: ISEE 3, *J. Geophys. Res.*, *87*, 632–642.
- Feldman, W. C., R. C. Anderson, S. J. Bame, S. P. Gary, J. T. Gosling, D. J. McComas, and M. F. Thomsen (1983a), Electron velocity distributions near the Earth's bow shock, *J. Geophys. Res.*, *88*, 96–110.
- Feldman, W. C., R. C. Anderson, S. J. Bame, J. T. Gosling, and R. D. Zwickl (1983b), Electron velocity distributions near interplanetary shocks, *J. Geophys. Res.*, *88*, 9949–9958.
- Feldman, W. C., R. M. Skoug, J. T. Gosling, D. J. McComas, and R. L. Tokar (1999), Observations of suprathermal electron conics in an interplanetary coronal mass ejection, *Geophys. Res. Lett.*, *26*, 2613–2616.
- Galvin, A. B., et al. (2008), The Plasma and Suprathermal Ion Composition (PLASTIC) investigation on the STEREO observatories, *Space Sci. Rev.*, *136*, 437–486, doi:10.1007/s11214-007-9296-x.
- Gary, S. P., B. Lavraud, M. F. Thomsen, B. Lefebvre, and S. J. Schwartz (2005), Electron anisotropy constraint in the magnetosheath: Cluster observations, *Geophys. Res. Lett.*, *32*, L13109, doi:10.1029/2005GL023234.
- Gosling, J. T., M. F. Thomse, S. J. Bame, and C. T. Russell (1989), Suprathermal electrons at Earth's bow shock, *J. Geophys. Res.*, *94*, 10,011–10,025.
- Gosling, J. T., S. J. Bame, W. C. Feldman, D. J. McComas, and J. L. Phillips (1993), Counterstreaming suprathermal electron events upstream of corotating shocks in the solar wind beyond ~2 AU: Ulysses, *J. Geophys. Res.*, *20*, 2335–2338.
- Gosling, J. T., R. M. Skoug, and W. C. Feldman (2001a), Solar wind electron halo depletions at 90° pitch angle, *Geophys. Res. Lett.*, *28*, 4155–4158.
- Gosling, J. T., D. J. McComas, R. M. Skoug, and R. J. Forsyth (2001b), Stream interaction regions at high heliographic latitudes during Ulysses's second polar orbit, *Space Sci. Rev.*, *67*, 189–192.
- Gosling, J. T., R. M. Skoug, and W. C. Feldman (2002), Symmetric suprathermal electron depletions on closed field lines in the solar wind, *Geophys. Res. Lett.*, *29*(12), 1573, doi:10.1029/2001GL013949.
- Gurnett, D. A. (1985), Plasma waves and instabilities, in *Collisionless Shocks in the Heliosphere: Reviews of Current Research*, *Geophys. Monogr. Ser.*, vol. 35, edited by B. T. Tsurutani and R. G. Stone, pp. 207–224, AGU, Washington, D. C.
- Horbury, T. S., P. J. Cargill, E. A. Lucek, J. Eastwood, A. Balogh, and M. W. Dunlop (2002), Four spacecraft measurements of the quasi-perpendicular terrestrial bow-shock: Orientation and motion, *J. Geophys. Res.*, *107*(A8), 1208, doi:10.1029/2001JA000273.
- Hull, A. J., J. D. Scudder, D. E. Larson, and R. Lin (2001), Electron heating and phase space signatures at supercritical, fast mode shocks, *J. Geophys. Res.*, *106*, 15,711–15,773.
- Kajdič, P., X. Blanco-Cano, A. Opitz, J.-A. Sauvaud, E. Aguilar-Rodriguez, C. T. Russell, J. G. Luhmann, L. K. Jian, A. P. Rouillard, and B. Lavraud (2013), Electron distributions upstream and downstream of ICME driven IP shocks, *AIP Conf. Proc.*, *1539*(1), 203.
- Lavraud, B., et al. (2010), Statistics of counter-streaming solar wind suprathermal electrons at solar minimum: STEREO observations, *Ann. Geophys.*, *28*, 233–246.
- Lemons, D. S., and W. C. Feldman (1983), Collisional modification to the exospheric theory of solar wind electron pitch angle distributions, *J. Geophys. Res.*, *88*, 6881–6887.
- Jian, L. K., C. T. Russell, J. G. Luhmann, A. B. Galvin, and K. D. C. Simunac (2013), Solar wind observations at STEREO: 2007–2011, *AIP Conf. Proc.*, *1539*, 191, doi:10.1063/1.4811020.
- Lin, R. P. (1998), Wind observations of suprathermal electrons in the interplanetary medium, *Space Sci. Rev.*, *86*, 61–78.
- Luhmann, J. G., et al. (2008a), IMPACT: Science goals and firsts with STEREO, *Adv. Space Res.*, *36*(8), 1534–1543, doi:10.1016/j.asr.2005.03.033.
- Luhmann, J. G., et al. (2008b), STEREO IMPACT investigation goals, measurements, and data products overview, *Space Sci. Rev.*, *136*, 117–184, doi:10.1007/s11214-007-9170-x.
- Maksimovic, M., et al. (2005), Radial evolution of the electron distributions functions in the fast solar wind between 0.3 and 1.5 AU, *J. Geophys. Res.*, *110*, A09104, doi:10.1029/2005JA011119.
- Masood, W., and S. J. Schwartz (2008), Observations of the development of electron temperature anisotropies in Earth's magnetosheath, *J. Geophys. Res.*, *113*, A01216, doi:10.1029/2007JA012715.
- Michell, J. J., S. J. Schwartz, and U. Auster (2012), Earth cross talk and asymmetric electron distributions near the Earth's bowshock, *Ann. Geophys.*, *30*, 503–513, doi:10.5194/angeo-30-503-2012.
- Montgomery, M. D., S. J. Bame, and A. J. Hundhausen (1968), Solar wind electrons: Vela 4 measurements, *J. Geophys. Res.*, *73*, 4999–5003.
- Ogilvie, K. W., R. Fitzenreiter, and M. Desch (2000), Electrons in the low-density solar wind, *J. Geophys. Res.*, *105*, 27,277–27,288.
- Page, C., S. P. Gary, C. A. de Koning, R. M. Skoug, and J. T. Steinberg (2007), Scattering of suprathermal electrons in the solar wind: ACE observations, *J. Geophys. Res.*, *112*, A04103, doi:10.1029/2006JA011967.
- Phillips, J. L., and J. T. Gosling (1990), Radial evolution of solar wind thermal electron distributions due to expansion and collisions, *J. Geophys. Res.*, *95*, 4217–4228.

- Phillips, J. L., W. C. Feldman, J. T. Gosling, C. M. Hammond, and R. J. Forsyth (1996), Suprathermal electron loss cone distributions in the solar wind: Ulysses observations, in *Proceedings of Solar Wind Eight*, vol. 382, edited by D. Winterhalter et al., pp. 293–296, Amer. Inst. Phys. Conf. Proceed., New York.
- Rosenbauer, H., H. Miggenrieder, M. Montgomery, and R. Schwenn (1976), Preliminary results of the HELIOS plasma measurements, in *Physics of Solar Planetary Environments*, edited by D. J. Williams, 319 pp., AGU, Washington, D. C.
- Russell, C. T., M. M. Mellott, E. J. Smith, and J. H. King (1983), Multiple spacecraft observations of interplanetary shocks: Four spacecraft determinations of shock normals, *J. Geophys. Res.*, *88*, 4793–4748.
- Saito, S., and S. P. Gary (2007a), All whistlers are not created equally: Scattering of strahl electrons in the solar wind via particle-in-cell simulations, *Geophys. Res. Lett.*, *34*, L01102, doi:10.1029/2006GL028173.
- Saito, S., and S. P. Gary (2007b), Whistler scattering of suprathermal electrons in the solar wind: Particle-in-cell simulations, *J. Geophys. Res.*, *112*, A06116, doi:10.1029/2006JA012216.
- Sauvaud, J.-A., et al. (2008), The IMPACT Solar Wind Electron Analyzer (SWEA), *Space Sci. Rev.*, *136*, 227–239, doi:10.1007/s11214-007-9174-6.
- Scudder, J. D., and S. Olbert (1979a), A theory of local and global processes which affect solar wind electrons 1. The origin of Typical 1 AU velocity distribution functions—Steady state theory, *J. Geophys. Res.*, *84*, 2755–2771.
- Scudder, J. D., and S. Olbert (1979b), A theory of local and global processes which affect solar wind electrons 2. Experimental support distribution functions—Steady state theory, *J. Geophys. Res.*, *84*, 6603–6619.
- Skoug, R. M., J. T. Gosling, D. J. McComas, C. W. Smith, and Q. Hu (2006), Suprathermal electron 90° pitch angle depletions at reverse shocks in the solar wind, *J. Geophys. Res.*, *111*, A01101, doi:10.1029/2005JA011316.
- Steinberg, J. T., J. T. Gosling, R. M. Skoug, and R. C. Wiens (2005), Suprathermal electrons in high-speed streams from coronal holes: Counterstreaming on open field lines at 1 AU, *J. Geophys. Res.*, *110*, A06103, doi:10.1029/2005JA011027.
- Štverák, Š., M. Maksimovic, P. M. Trávníček, E. Marsch, A. N. Fazakerley, and E. E. Scime (2009), Radial evolution of non-thermal electrons in the low-latitude solar wind: Helios, Cluster and Ulysses observations, *J. Geophys. Res.*, *114*, A05104, doi:10.1029/2008JA013883.
- Vocks, H., and G. Mann (2003), Generation of suprathermal electrons by resonant wave-particle interaction in the solar corona and wind, *Astrophys. J.*, *593*, 1134–1145.
- Vocks, H., C. Salem, R. P. Lin, and G. Mann (2005), Electron halo and Strahl formation in the solar wind by resonant interaction with whistler waves, *Astrophys. J.*, *627*, 540–549, doi:10.1086/430119.
- Walker, S. N., M. A. Balikhin, H. St. C. K. Alleyne, Y. Hobar, M. André, and M. W. Dunlop (2008), Lower hybrid waves at the shock front: A reassessment, *Ann. Geophys.*, *26*, 699–707.
- Zaslavsky, A., et al. (2012), Interplanetary dust detection by radio antennas: Mass calibration and fluxes measured by STEREO/WAVES, *J. Geophys. Res.*, *117*, A05102, doi:10.1029/2011JA017480.